Construction and Building Materials 495 (2025) 143660

Contents lists available at ScienceDirect

Construction and Building Materials

journal homepage: www.elsevier.com/locate/conbuildmat

Effect of scallop shell powder addition on fresh and hardened properties of self-compacting concrete (SCC) based on recycled aggregates

Meriem Guessoum [a,*], Bouha El Moustapha [a], Fouzia Khadraoui [a], Daniel Chateigner [b], Stéphanie Gascoin [b], Walid Maherzi [c]

[a] Builders Ecole d'Ingénieurs, Unité de Recherche "Builders Lab", ComUE NU, Campus Caen, Epron, France
[b] CRISMAT-ENSICAEN, UMR CNRS 6508, Université de Caen, Normandie, IUT Caen, Normandie Université, 6 Boulevard Maréchal juin, Caen 14050, France
[c] Department of Civil Engineering and Environmental, IMT Lille Douai, EA 4515 – LGCgE, University of Lille, Lille F 59000, France

ARTICLE INFO

Keywords:
Self-compacting concrete
Limestone powder
Scallop shell powder
Recycled coarse concrete aggregates
Fresh properties
Hardened properties

ABSTRACT

This study examines scallop shell powder (SSP) and recycled coarse aggregates (RCA) as alternatives to limestone powder (LS) and natural coarse aggregates (NCA) in self-compacting concrete (SCC). SSP improved viscosity and segregation resistance with minimal slump loss, induced progressive pore coarsening as revealed by MIP, and reduced 90-day compressive strength. RCA reduced wet density, limited workability retention to 45 min, and decreased compressive strength by up to 11 %, while increasing porosity and absorption. Despite this reduction in mechanical performance, the combined use of SSP and RCA promotes waste recovery and resource conservation, thereby contributing to a more sustainable SCC.

1. Introduction

Waste generation, CO_2 emissions, and the extensive extraction of non-renewable natural resources are among the principal environmental consequences of industrial activities. Undoubtedly, the construction sector leads the industrial sectors in these impacts. In France, cumulative CO_2 emissions associated with cement production in 2022 reached 713.46 million tons (Mt) of CO_2, compared to the world's cumulative CO_2 emissions of around 46 billion tons [1]. Additionally, around 360 Mt of aggregates (sand and gravel), limestone powder (LS), and gypsum are extracted annually in France [2]. Beyond CO_2 emissions and resource extraction, the French construction sector generates around 70 % of the country's total annual waste, amounting to approximately 227.5 million tons, of which 49 % comes from demolition [3].

Considering these concerns, shellfish farming wastes, including Pacific oysters (*Crassostrea gigas*), king scallops (*Pecten maximus*), and blue mussels (*Mytilus edulis*), emerge as a suitable alternative to LS [4–7]. Every year, more than 10 million tons of shellfish waste are generated, over 70 % of which comes from the species mentioned earlier.[8]. Similarly, recycled coarse aggregates (RCA) are being adopted as substitutes for natural coarse aggregates (NCA), offering substantial potential for reducing natural aggregate consumption and promoting sustainable waste management [9].

However, an in-depth assessment of the effects of alternative materials on concrete performance is essential before their use in industrial-scale applications. This study focuses on self-consolidating or self-compacting concrete (SCC) due to its extensive and increasing use in the construction industry, driven by the enhanced productivity, efficiency, and overall construction quality that it can provide [10]. The exceptional flowability of SCC allows it to consolidate under its own weight without requiring external vibration [11]. Alongside this property, stability and workability retention are key for the precast industry. However, these properties are disturbed by plastic stiffness caused by water loss, structural build-up, or thixotropy [12]. They also depend on the particle size distribution, the water absorption capacity of aggregates, ambient conditions, time, the interaction of the Supplementary Cementitious Materials (SCM) with water, cement chemistry, and cement-superplasticizer (SP) compatibility. In this context, the physical properties of SSP and RCA play a critical role in SCC rheological behavior. As reported, the surface roughness of SSP, compared to LS,

Abbreviations: SCC, Self-consolidating or self-compacting concrete; SCM, Supplementary Cementitious Materials; SSP, Scallop shell powder *P. maximus*; LS, Limestone powder; RCA, Recycled coarse concrete aggregates; NCA, Natural coarse aggregates; SP, Superplasticiser; PCS, Polycarboxylate superplasticizer; SA, Set Accelerator; ITZ, Interfacial transition zone; SR, Static segregation.

* Corresponding author.
E-mail address: meriem.guessoum@builders-ingenieurs.fr (M. Guessoum).

https://doi.org/10.1016/j.conbuildmat.2025.143660
Received 11 June 2025; Received in revised form 30 August 2025; Accepted 14 September 2025
Available online 18 September 2025
0950-0618/© 2025 Elsevier Ltd. All rights are reserved, including those for text and data mining, AI training, and similar technologies.

provides a larger surface area, which enhances SCC cohesion and helps reduce bleeding, segregation, and thixotropy [13,14]. In contrast, the smooth and flat surface texture of LS [15] increases the friction forces between solid particles, the plastic viscosity, the thixotropy, and the yield stress, consequently reducing the slump flow [16].

Regarding RCA, their high water absorption capacity and rough surface texture, compared to NCA, increase the yield stress, reducing SCC workability [17–19]. Bleeding, segregation, and slump flow strongly depend on the moisture state of RCA. For instance, saturated surface dry RCA initially increases the cumulative bleeding of SCC but tends to stabilize rapidly after 45 min [20]. In contrast, air-dry RCA, with a water compensation technique, increases the effective w/c ratio of SCC, thereby enhancing flowability and cumulative bleeding [21].

Concerning waste effects on hardened SCC properties, SSP (like LS) exhibits the lowest reactivity among other SCM and is primarily composed of the calcite mineral phase, the most thermodynamically stable calcium carbonate among other polymorphs [22]. Meanwhile, seashells in general consist of a mixture of calcite and aragonite, with the aragonite content varying between different seashell types [23]. SSP is typically composed of calcite, with only trace amounts of aragonite [24]. Several studies highlighted the chemical reaction of LS and SSP with the aluminate phases (C_3A), forming hemicarboaluminate (Hc) and monocarboaluminate ($C_3(A,F)\cdot CaCO_3\cdot 11\ H_2O$ (Mc)). These reactions stabilize the conversion of ettringite into monosulfate, thereby enhancing the hydration rate and the cement matrix packing density, contributing to increased compressive strength [25]. Further, LS exhibits a more privileged surface for nucleation and hydrate growth when compared with Other SCM from SSP, for instance, quartz [26]. The potential of ground seashells to act as nucleation sites for hydration product growth is proportional to their calcite content, since this latter exhibits protruding oxygen atoms and calcium atom sub-lattices at its cleavage plane [27]. Aragonite's surface, on the other hand, is stably terminated with only Ca, leading to a weaker nucleation effect [28,29]. Although LS and SSP possess a similar chemical composition, the organic matter in SSP may terminate grain surfaces, inhibiting the crystal growth [30]. Turning our attention to RAC, their tendency to absorb more water during the mixing phase of concrete may disturb the cement-water ratio (w/c), negatively impacting both the rheological behavior of the concrete and cement hydration [31]. The presence of RCA induces two interfacial transition zones (ITZs), compared to natural NCA, which only forms a single ITZ, leading to increased heterogeneity, higher porosity, and reduced strength [19]. Moreover, the porous residual matrix on RCA reduces bulk density [32], resulting in a linear decrease in fresh concrete density with increasing RCA content [33,34]. Eventually, the hardened properties of RCA concrete are strongly influenced by the intrinsic characteristics of the RCA itself, including the porosity, density, and quality of its former adherent mortar [35]. This explains the observed variability in the properties of concrete incorporating these aggregates.

Although SSP may theoretically exhibit similar effects to LS, there is a noticeable lack of direct experimental studies evaluating its potential as a sustainable substitute in SCC incorporating 100 % RCA. Furthermore, several uncertainties continue to hinder the widespread adoption of RCA in SCC, specifically the variability in physical and mechanical properties of industrial-grade RCA and its consequent impact on fresh and hardened concrete performances.

Accordingly, this study is dedicated to examining the combined effect of SSP and 100 % RCA on the fresh properties of SCC and the evolution of its hardening properties over the 90 days of curing. Several characterizations of SCC are carried out in this study. Fresh properties were evaluated through workability retention, resistance to segregation, wet density, and hydration heat. Hardened properties were examined through compressive strength, microstructural analysis (TGA/DTG and SEM), accessible porosity, bulk density, and pore structure using mercury intrusion porosimetry (MIP).

Table 1
PCS and SA characteristics.

	PCS	SA
Density (g/cm^3)	1.06 ± 0.03	1.39 ± 0.03
Dry extract (%)	30.0 ± 1.50	42.65 ± 2.25
pH	5.50 ± 1.70	8.0 ± 2.0

2. Materials and methods

2.1. Materials

2.1.1. Binders

The study uses two binder systems: the first system consists of CEM II/A-LL 52.5 N CE PM-CP2 NF cement from the Heidelberg Cement Group, France, combined with LS from Omya International AG, France. The second system also combines the same cement with SSP, provided in its shell form by Ovive, France. Initially, the shells were washed with tap water and scrubbed using a wire brush to remove salt residues and any remaining biomass, then ground for 4 h using a TM500 drum mill from RETSCH©, with a rotation speed of 45 rpm and a ball/material mass ratio of 3/1. The grounded SSP is then sieved through a 120 μm sieve to collect particles with a maximum size of 125 μm, comparable to that of LS.

2.1.2. Aggregates

A washed siliceous alluvium sand with a nominal size range of 0–4 mm is used as the fine aggregate. The sand is sourced from Sablière Route des Sables – Le Haut-Lieu, France. Two coarse aggregates are used: semi-crushed silico-calcareous alluvium NCA from Carrière STREF & Cie (Jumièges) and RCA from Carrière de la Roche Blain, France. Both coarse aggregates exhibit a similar size fraction of 4/12.5. The RCA are classified as Rcug= 86 % and X = 1 %, according to EN 933–11 [36].

2.1.3. Admixtures

Two types of admixtures, commercialized by BASF company, are incorporated during the mixing phase of the SCC mixes: a polycarboxylate superplasticizer (PCS) and a Set Accelerator (SA), primarily to facilitate the demolding process for a subsequent study. Their characteristics are summarized in Table 1

2.2. SCC mix designs

For the experiment, four SCC mixes were produced. The control SCC consists of a binder with 30 % LS and 70 % cement II-52.5 N, with 100 % NCA (LS-NCA) by volume, and was designed using the BétonlabPro software, with the following basic parameters: C = 320 kg per cubic meter of SCC with a strength class of C 30/37, a target consistency class SF2 (660–750 mm), a viscosity class VS1 ($t_{500} < 2.0$ min), and a segregation resistance class SR1 (≤ 20 %). The first SCC test mix includes the same binder composition with 100 % RCA (LS-RCA). The second test mix contains 30 % SSP with 70 % cement and 100 % NCA (SSP-NCA),

Table 2
Mix proportions per cubic meter of SCC.

Constituents (kg/m^3)	SCC			
	LS-NCA	LS-RCA	SSP-NCA	SSP-RCA
Sand 0/4	847.77	847.77	842.11	842.11
NCA 1/12.5	719.14	-	714.34	-
RCA 4/12.5	-	646.06	-	641.75
CEM II−52.5 N	320	320	320	320
LS	137.5	135.7	-	-
SSP	-	-	137.5	137.5
Water $_{tot}$	219.6			
PCS	4.58			
SA	3.66			

and the third test mix contains the same binder but 100 % RCA (SSP-RCA). The other components remain constant in volume across all mixes. The 30 % filler content and the use of 100 % RCA were selected based on a reference SCC formulation developed and validated in previous research, in which this combination (30 % LS and 100 % RCA) demonstrated satisfactory performance and was subsequently implemented in an industrial application [37]. Moreover, a 30 % replacement of cement with SSP has also been recommended in the literature[38]. The formulations were optimized based on a coarse aggregate-to-sand (G/S) ratio of 0.9, a filler content between 120 and 200 kg per cubic meter of SCC, and a superplasticizer (SP) dosage close to its saturation point. Table 2 summarizes the four SCC mix compositions.

2.3. Mixing method and curing conditions

Before mixing the SCC mixes, the aggregates were dried at 60 °C and cooled to room temperature. The water compensation method was used to achieve a slump flow class of SF2 and to account for water loss due to the RCA's high water absorption capacity. The additional water was determined empirically through preliminary trial mixes and was adjusted incrementally until the target slump flow and workability of the SCC mix were achieved. This method is recommended in the literature, as it enhances the compressive strength of concretes containing RCA and ensures consistency in slump measurements [39,40]. All SCC mixes were blended for 3 min in a laboratory mixer at 17 ± 3 °C, including 30 s of dry mixing, 30 s of mixing with one-quarter of the total mixing water mixed with PCS and SA, and 2 min with the remaining water. Immediately after mixing, the fresh SCC mixes were evaluated for workability retention, segregation resistance, wet density, and hydration heat. These were then cast into cubic specimens measuring 10 cm× 10 cm x 10 cm, de-molded after 24 h of casting, and cured in water at 20 °C and 95 % relative humidity for 1, 7, 28, and 90 days. The hardened specimens were studied using compressive strength tests, microstructural analysis using SEM imaging, thermal behavior using TGA/DTG, accessible porosity, bulk density, and pore structure using mercury intrusion porosimetry (MIP).

2.4. Methods

2.4.1. Raw materials characterization

The physical and mechanical properties of the coarse aggregates were characterized through standardized tests: water absorption kinetics and density, measured according to NF EN 1097–6 [41]; sieve analysis was carried out according to NF EN 933–1 [42]; and resistance to fragmentation and wear was further assessed using the Los Angeles (LA) abrasion and the Micro-Deval (MDE) tests, conducted according to NF EN 1097–2 [43] and NF EN 1097–1 [44], respectively.

The particle density and Blaine specific surface area of cement, LS, and SSP were determined according to NF EN 1097–7 [45] and EN 196–6 [46], while Rigden voids and loss on ignition were measured following NF EN 1097–4 [47] and NF EN 15935 [48], respectively.

The particle size distribution of the binder constituents was determined using a Beckman Coulter LS13320 laser diffraction granulometer, operating on the principle of light scattering according to ISO 13320–1 [49]. For the < 124 125 μm SSP and LS particles, the powders were dispersed in water and analyzed while kept in suspension with a stirred bath to avoid settling of coarse particles. For cement, measurements were performed using a dry dispersion unit to prevent any premature hydration.

Scanning Electron Microscopy (SEM) analysis was performed to examine the particle morphology of SSP and LS particles. The analyses were carried out using a Carl ZEISS SUPRA 55 microscope in secondary electrons mode, with an applied voltage of 3 kV, a 60 μm diaphragm aperture, and a working distance of 3–5 mm to avoid charging as much as possible. The observations were performed on non-coated bulk samples glued with carbon conductive tape on the pad and surrounded with silver lacquer. SEM was also employed to investigate the ITZ structure and the packing density of the fragmented SCC samples at different curing ages. The samples were immersed in acetone to stop cement hydration until the day of analysis.

The X-ray diffraction (XRD) measurements were conducted using an X'Pert Pro Panalytical diffractometer operating with Co Kα1/Kα2 radiation (λKα1 = 1.789010 Å and λKα2 = 1.792900 Å) and equipped with an X'Celerator detector, in the θ–2θ recording mode. Patterns were recorded in the 2θ range from 5° to 120° with a scan step of 0.016° (2θ). The crystalline phases present in SSP, LS, and the residual mortar of RCA were identified. The residual mortar was detached from the aggregates, ground using a mortar and pestle, and sieved to < 63 μm. The entire profile refinements were performed following the Rietveld method using MAUD (Materials Analysis Using Diffraction) software.

The thermogravimetric analysis (TGA) of SSP and LS was conducted using a thermo-gravimetric analyzer Jupiter STA 449 F5 to evaluate their thermal stability and decomposition behavior. The analysis involves continuously recording the mass variations of the powders as the temperature increases from 25 °C to 1200 °C at a heating rate of 10 °C/min under a nitrogen atmosphere. The same analysis was also performed on the ground and sieved (<63 μm) acetone-preconditioned SCC samples for microstructural analysis. For all measurements, approximately 170 mg of sample was used. All experimental tests were carried out at room temperature, i.e., between 19 °C and 21 °C.

Table 3
VSI Scale for SCC [51].

VSI Scale	Observation	SCC stability
0	No evidence of segregation in the slump flow patty, mixer drum, or wheelbarrow	Highly stable mix
1	No mortar halo in the slump flow patty, but some slight bleeding on the surface of concrete in mixer drum and/or wheelbarrow	Stable mix
2	Slight mortar halo (< 10 mm) in slump flow patty and noticeable layer of mortar on surface of testing concrete in mixer drum and wheelbarrow	Unstable mix
3	Clearly segregating by evidence of large mortar halo (> 10 mm) and thick layer of mortar and/or bleed water on surface of testing concrete in mixer drum or wheelbarrow	Highly unstable mix

2.5. Fresh properties

2.5.1. Workability retention: Slump flow test

The slump flow test following NF EN 12350–8 [50] assesses the SCC mixes' workability retention. The test proceeds at four intervals: t = 0, t = 15 min, t = 45 min, and t = 90 min. For triplicate batches, the final spread diameter is determined as the average of two orthogonal diameters. Additionally, the time required to achieve a spread diameter of 500 mm, indicating the material's viscosity, denoted as t_{500}, is recorded.

2.6. Segregation resistance

2.6.1. Visual Stability Index (VSI)

Two operators visually inspect the formed SCC spreads at the end of the flow to determine the VSI. Table 3 provides the VSI scale for evaluating the static and dynamic stability of SCC [51].

2.6.2. Sieve segregation test

The resistance of SCC to the static segregation (SR), which indicates its ability to keep particles suspended without settling due to gravity, is assessed using the sieve segregation test following NF EN 12350–11 [52] and calculated using the equation (Eq. 1).

$$SR = \frac{(m_{ps} - m_p) \times 100}{m_c} \quad (1)$$

Where:

- SR: segregated fraction in weight percent.
- m_{ps}: the total mass (sieve receiver plus passed material).
- m_p: the mass of the sieve receiver.
- m_c: the initial mass of SCC placed onto the sieve.

2.6.3. Wet density

The wet density was determined following NF EN 12350–6 [53], and calculated using (Eq. 2).

$$D = \frac{m_2 - m_1}{V} \quad (2)$$

Where:

- D: wet density of the fresh concrete.
- m_1: mass of the empty container.
- m_2: mass of the container filled with concrete.
- V: volume of the container.

2.6.4. Heat of hydration

The heat of hydration of the SCC mixes is measured according to NF EN 196–9 [54], using a semi-adiabatic method, Langavant type, for 72 h. After 3 min of mixing, the SCC was poured into the cylindrical metal container and placed inside the insulated calorimeter. The heat of hydration (Q) and the instant hydration heat are measured using (Eq. 3).

$$Q(J/g) = \frac{c}{m_c}\Theta_t + \frac{1}{m_c}\int_0^t \alpha \times \Theta_t \times dt \quad (3)$$

Where:

- c: total thermal capacity of the calorimeter, in J K^{-1}
- m_c: mass of cement contained in the test sample, in g.
- t: hydration time, in h.
- α: coefficient of heat loss of the calorimeter in J h^{-1} K^{-1}.
- Θ_t: difference in the temperature of the test calorimeter compared with that of the reference calorimeter at time t, in K.

2.7. Hardened properties

2.7.1. Compressive strength

The hardening properties of the six specimens are determined using a compression strength test according to NF EN 12390–3 [55] on a 3 R© compression machine with a capacity of 4000 kN and a loading speed of 0.6 MPa.s^{-1}.

2.7.2. Bulk density, porosity accessible to water, and water absorption

The water-accessible porosity, water absorption, and apparent density of the hardened SCC are evaluated according to NF P 18–459 [56]. The test involves placing the nine specimens under a vacuum at a pressure of 25 mbar for the first 4 h, followed by 44 h in water, with the pressure remaining constant. The bulk density (ρ_d), expressed in kg/m^3, the porosity accessible to water (ε), expressed as a volumetric percentage, and the water absorption (w) are then calculated using (Eq. 4, Eq. 5, and Eq. 6), respectively.

$$\rho_d = \frac{M_{air}}{M_{air} - M_{water}} \times 100 \quad (4)$$

$$\varepsilon(\%) = \frac{M_{air} - M_{dry}}{M_{air} - M_{water}} \times 100 \quad (5)$$

$$w(\%) = \frac{M_{water} - M_{dry}}{M_{dry}} \times 100 \quad (6)$$

Where:

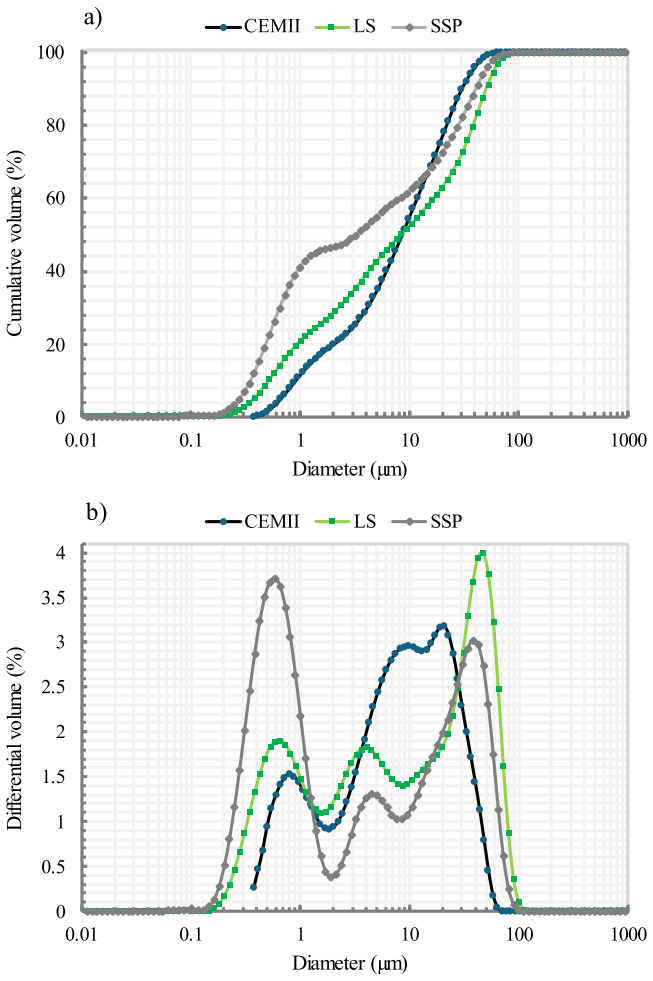

Fig. 1. Particle size distribution of the binder components.

- M_{air}: mass of the saturated sample in air.
- M_{water}: mass of the specimen submerged in water.
- M_{dry}: mass of the dried specimen at 105 °C, or 60 °C for SCC containing RCA, until constant weight is reached.

2.8. Microstructural characterization

2.8.1. Thermogravimetric analysis

The analysis aims to quantify the hydrated phases, primarily C-S-H and portlandite $Ca(OH)_2$, within the temperature range corresponding to their dehydration and dihydroxylation. The onset of the bound water loss is considered to occur at 150 °C. From this point up to the onset of $Ca(OH)_2$ dihydroxylation at around 400 °C, the observed mass loss is attributed to the decomposition of gypsum, ettringite, and carboaluminate hydrates [57,58]. However, the water loss within this temperature range is mainly due to C-S-H dehydration. Therefore, in this study, all hydration products contributing to the mass loss between 150 °C and 400 °C are collectively grouped under the notation C-S-H, and the weight loss located between 400 °C and 525 °C corresponds to $Ca(OH)_2$ dihydroxylation. The C-S-H and $Ca(OH)_2$ amounts are estimated using (Eq. 7 and Eq. 8), respectively [59].

$$C-S-H(\%) = \Delta m_{150\,^\circ C - 400\,^\circ C} \times \frac{MW_{C-S-H}}{S \times MW_{H_2O}} \quad (7)$$

$$Ca(OH)_2 \quad (\%) = \Delta m_{400\,^\circ C - 520\,^\circ C} \times \frac{MW_{Ca(OH)_2}}{MW_{H_2O}} \quad (8)$$

Where:

Table 4
Physical Properties of Binder Components.

	Cement	LS	SSP
Density (g/cm^3)	3.11	2.70	2.50
Blaine specific surface area (cm^2/g)	4436	6110	6450
Average grain size (μm)	41.04	10.20	3.90
Loss on ignition at 550 °C (%)	-	0.50	1.60
Rigden voids (%)	-	25	34

– MW: C-S-H, $Ca(OH)_2$, and H_2O molecular weight.
– S: number of moles of water involved in C-S-H dehydration.

The chemical composition of C-S-H is approximately $1.7CaO{\cdot}SiO_2 4\ H_2O$, which at equilibrium tends to be $1.7CaO{\cdot}SiO_2 2.1\ H_2O$ [60, 61]. Therefore, we assume the chemical composition of C-S-H considered in this study is $1.7CaO{\cdot}SiO_2 2.1\ H_2O$.

2.8.2. Pores analysis: Mercury intrusion porosimetry (MIP) test

The total porosity and pore size distribution measurements were conducted using the MIP method, in accordance with ISO 15901–1 [62], using a Micromeritics AutoPore V 9600 porosimeter. The instrument performs low-pressure measurements ranging from 0 to 345 kPa, corresponding to pore sizes between 360 μm and 3.6 μm. It also conducts high-pressure measurements from atmospheric pressure up to 228 MPa, covering pore sizes from 6 μm down to 0.005 μm.

3. Results and discussion

3.1. Raw materials characterization

3.1.1. Binders

Particle size distribution of the binder components. Fig. 1.a illustrates the particle size distribution of cement, LS, and the ground SSP, determined using a laser diffraction particle size analyzer (Beckman Coulter, LS13 320). SSP has a higher fraction of ultrafine particles, with about 40 % of its particles' volume ranging below 1 μm in size, compared to LS and cement, with 20 % and 10 %, respectively. However, above 10 μm in size, both LS and SSP exhibit coarser particles than cement (Fig. 1.b), with a mean size of around 40 and 50 μm, respectively. A comparison of these particle size distributions indicates that, on an overall, while particle sizes for cement are dominantly distributed in an intermediate range from 2 to 40 μm, the volume fractions of LS and SSP are either finer than 2 μm or larger than 40 μm for their major contributions. The observed distributions result in mean sizes typically 10 and 4 times larger for cement compared to LS and SSP respectively (Table 4) with a lower density for the latter. The lower density of SSP is accompanied by a larger specific surface of the grains, as seen from Blain values, and correlated with the Rigden voids values.

Particle morphology of LS and SSP: SEM images of the LS and SSP particles (Fig. 2) illustrate some of their characteristic features and morphology. The largest LS particles (Fig. 2.a) mostly exhibit plate-like shapes, with smooth surfaces and rather well-defined edges. They appear compact with only a few surface steps that signify the existence of subdivisions, either from first- or second-order lamellae, originating from ancient shells from Brachiopoda or Mollusca lithified through

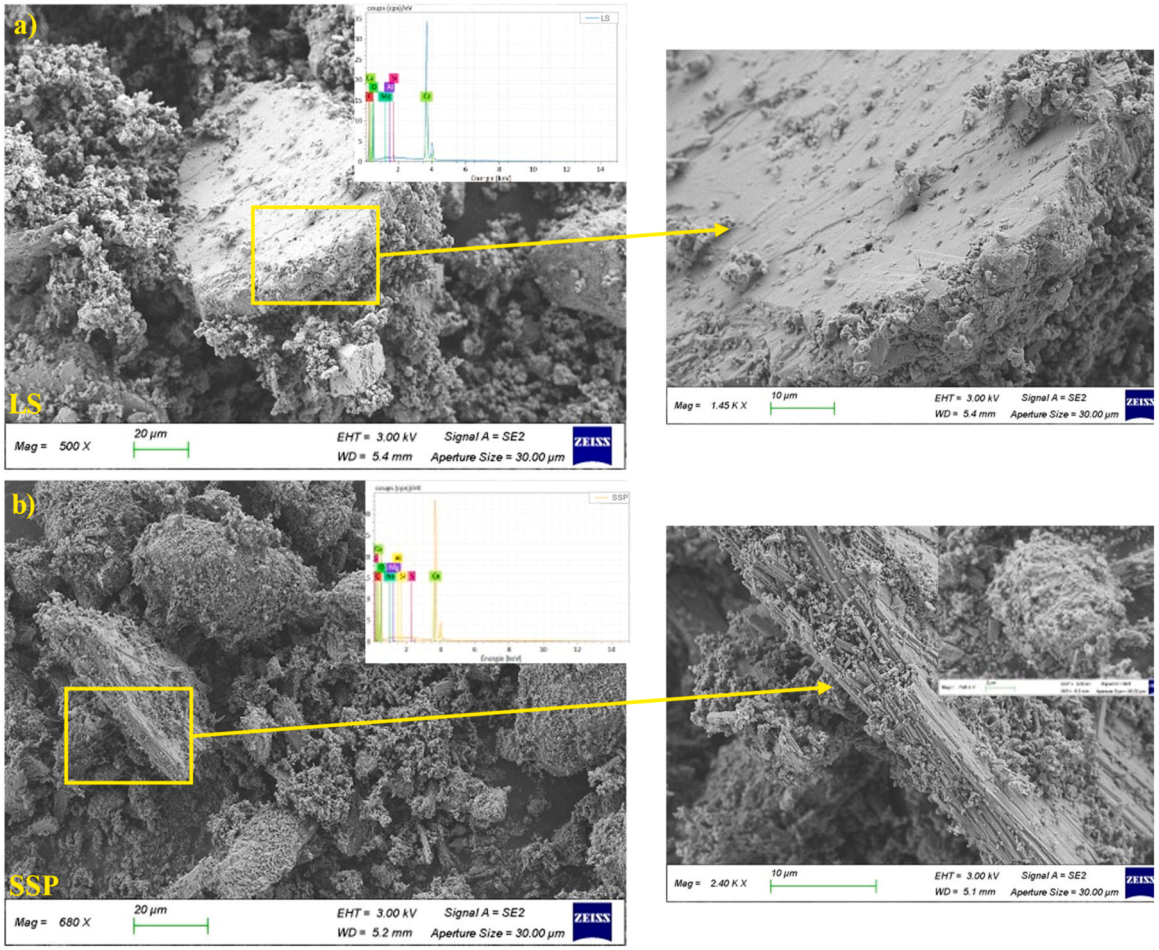

Fig. 2. Backscattering SEM images of the a) LS and b) SSP powders.

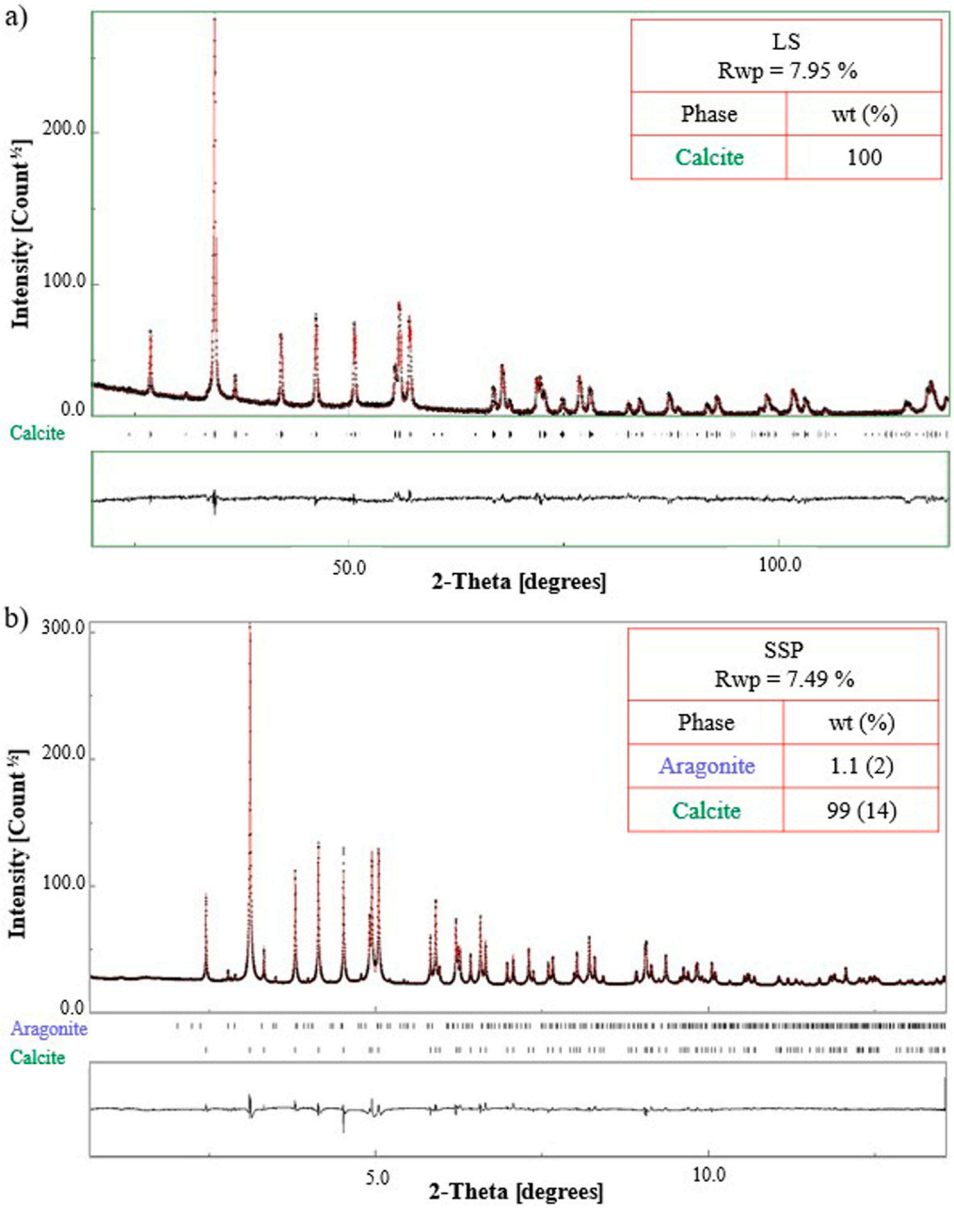

Fig. 3. XRD patterns of a) LS and b) SSP powders.

metamorphic processes [63]. The ground LS powder shows fewer signs of fine-particle agglomeration than SSP. In contrast, the SSP particles are more irregular and granular (Fig. 2.b), often appearing as clusters or schistous structures [64]. They exhibit rougher surfaces and more porosity, with a noticeable aggregation of finer particles. At larger magnification, the SSP SEM images reveal the original lamellae system from *P. maximus* shells [24]

X-ray diffraction analysis (XRD) of LS and SSP. The XRD patterns of LS (Fig. 3.a) and SSP (Fig. 3.b) indicate calcite as the dominant mineralogical component in both powders, with traces of aragonite detected in SSP.

Thermogravimetric analysis (TGA/DTG). TGA weight losses (Fig. 4) for both precursor powders show a significant mass loss occurring in the 726 °C-1000 °C temperature range. This mass loss corresponds to the $CaCO_3$ decomposition, which releases CO_2 [59], a classically observed phenomenon for samples mainly composed of $CaCO_3$. However, the decomposition peak in the DTG curve of SSP appears at 905 °C, 20 °C lower than that of LS, at 925 °C. The difference in decomposition temperature between the two samples might be a priori associated with various factors: grain sizes, carbonate polymorphs, crystallinity, and organic contents in the sample. However, both samples of $CaCO_3$ exhibit a calcite signature and similar grain size distributions. But, SSP clearly contains intra- and inter-crystalline organic molecules, as usual in mollusk shells, within an around 1–2 wt% range. Such molecules, responsible for the shell growths into oriented patterns and giving rise to unit-cell distortion of the mineral matrix, are much less able to resist high temperatures [65]. Their decomposition arises in the 200–400 °C range, explaining the quite different evolution of the DTG curve below 500 °C, compared to that of the LS samples (zoom of the corresponding range in (Fig. 4). These observations align with the loss on ignition at 550 °C values for both SSP and LS samples (Table 4).

3.1.2. Aggregates

The absorption kinetics of the coarse aggregates are presented in Fig. 5.a. RCA exhibit an absorption capacity approximately twice that of NCA, nearly stable over time. The sieve analysis results, shown in Fig. 5. b, indicate that while sand grain sizes range between 0.1 and 1.3 mm, those of NCA and RCA display very close distributions and typically ten

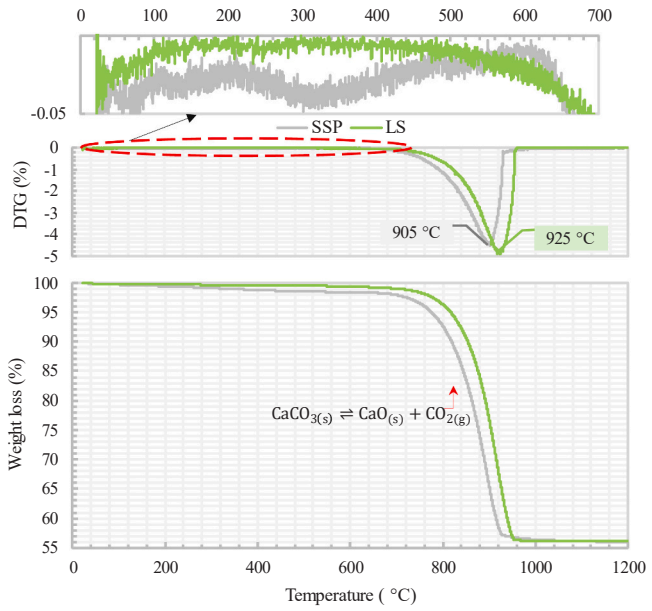

Fig. 4. TGA and DTG curves for LS and SSP powders and zoom of the DTG curves below 700 °C (top plots).

times larger sizes between 3 and 14 mm. Table 5 presents other physical and mechanical properties of the used aggregates. A large difference in resistance to abrasion and fragmentation between NCA and RCA, the latter exhibiting relatively low mechanical properties in the corresponding tests.They also exhibit a density approximately 10% lower than that of NCA.

Surface morphology of NCA and RCA. The NCA grain surfaces exhibit relatively low porosity (Fig. 6.a), a denser texture, and no residual material, compared to the rougher RCA grain surfaces (Fig. 6.b) due to the presence of adhered old mortar.

Old mortar composition. The adhered old mortar is composed of major mineral phases, quartz and calcite, alongside minor constituents such as vaterite, albite low, muscovite, and chlorite, as well as trace amounts of orthoclase and aragonite (Fig. 7.a). Additionally, the TGA and DTG analyses indicate the presence of $CaCO_3$ and C-S-H phases within the adherent mortar, while $Ca(OH)_2$ is notably absent, suggesting its consumption during the natural carbonation of RCA (Fig. 7.b).

3.2. Fresh properties

3.2.1. Workability retention: Slump flow test

Workability retention tests (as seen from slump flow and t_{500} values) are measured for up to 90 min after the mixing phase, and the results are plotted in Fig. 8, revealing consistent trends for all mixes. Regarding only the NCA mixes (Fig. 8.a and b), both mixes show similar spread flow values, which tend to decrease over time, but remain close to the SF2 range after 90 min of mixing, 65 cm for NCA-LS and 62 cm for NCA-SSP. These trends are consistent with previous findings [19,20,37,66]. However, the difference in behavior between LS-NCA and SSP-NCA is more pronounced, looking at the t_{500} values, which increase much more rapidly in the mix containing LS. The observed differences can be attributed to the higher content of ultrafine particles in SSP, which fill most of the voids and displace excess water (dilution effect), thereby resulting in lower viscosity values [67,68].

When substituting NCA with RCA, the flowability and workability retention period decreases to approximately 45 min, due to an increase in viscosity. At this point, the PCS begins to lose effectiveness, as the differences between the mixes become more evident [69]. It is reported that SP initially gives a good dispersion effect, typically from 20–30 min, before slump loss persists, due to its adsorption onto cement and filler

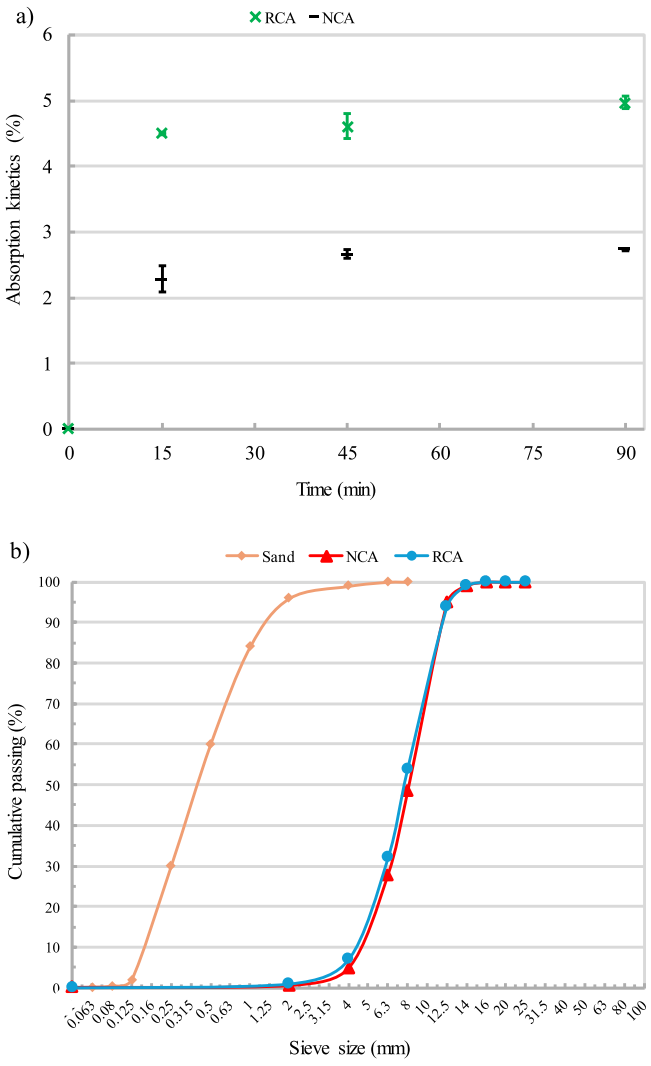

Fig. 5. a) Water absorption kinetics in NCA and RCA, and b) corresponding grain size distributions, including sand obtained from sieving.

Table 5
Physical and mechanical properties of aggregates.

Aggregate	LA (%)	MDE (%)	ρ (g/cm^3)	w_{24} (%)
Sand	-	-	2.61	0.40 ± 0.08
NCA	16	4	2.46	2.71 ± 0.16
RCA	31.16	46.6	2.21	5.46 ± 0.13

surfaces [70,71]. After 90 min, LS- RCA loses around 44 % of the initial spread flow, 28 %, and 11 % higher than LS- NCA and SSP- RCA, respectively. The porous surface of RCA, its high water absorption capacity, and the dry state of RCA modify the rheology of SCC. As can be seen from (Fig. 5.a), at 24 h, RCA exhibits an absorption coefficient of around 5 %, which is two times larger than that of NCA. Within 15 min of water immersion, around 82 % of the 24-hour absorption value is reached for RCA, a behavior that has also been observed in earlier studies [19,72]. However, despite the accentuated loss in the flowability of the mix containing LS, which also did not get the t_{500} by 90 min, the roughness of the old cementitious matrix surrounding the RCA might counterbalance some of the increased viscosity and the yield stress by ensuring that the aggregates are well coated with the cementitious paste and less likely to settle [69,73]. As a result, the homogeneity and its thixotropic behavior are improved. Similar effects were previously observed with air-dried RCA combined with a water compensation

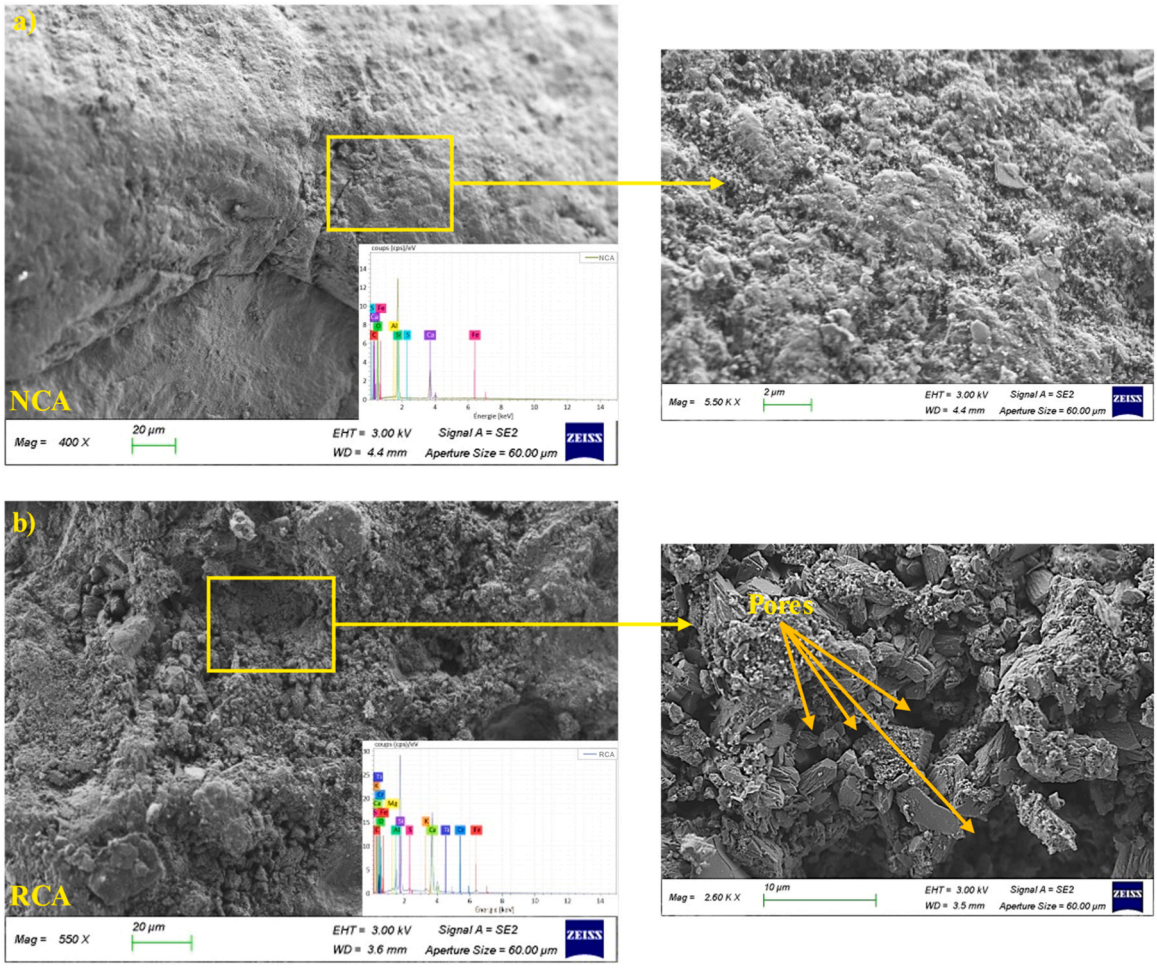

Fig. 6. SEM backscattered images of the a) NCA and b) RCA surfaces.

technique, which improved flowability and cumulative bleeding [21, 74].

3.3. Segregation resistance

3.3.1. Visual Stability Index (VSI)

Among the four fresh mixes, the LS-NCA exhibits the highest VSI, as shown in Table 6. Once the mix reaches its final spread, the aggregates settle rapidly, leaving a top layer richer in paste, with a slight mortar halo in the slump flow patty. Similar results have been previously reported [17,75]. Moreover, during standing periods between successive testing intervals, the considered mix behaves differently, demonstrating a significantly higher thixotropic aspect and excessive bleeding than its counterparts with RCA and the SSP mixes.

3.3.2. Sieve segregation

The experimental results of the sieve segregation test are plotted in Fig. 9, reveling that all mixes exhibit a SR1 segregation-resistance class. As expected, the LS-NCA mix, which exhibited noticeable bleeding, also showed poor resistance to segregation. Its SR value is around 4 % higher than that of SSP-NCA. More importantly, these tests further reveal that the presence of RCA in SCC improves its resistance to segregation. The observed behavior is consistent with findings previously reported [34, 76,77].

3.3.3. Wet density

Regarding the SCC mixes' wet density illustrated in Fig. 10.a, the LS-NCA mix exhibits the highest wet density of 2303 kg/m^3, among the four mixes. The latter decreases to 2289 kg/m^3 when substituting NCA with RCA. SSP-NCA demonstrated a further reduction at 2280 kg/m^3 , when the lowest value, 2249 kg/m^3, is recorded for SSP-RCA. The decreasing trend in density is mainly attributed to the lowest density of RCA and SSP compared to NCA and LS. This trend aligns with previously observed trends showing a linear decrease in density as the substitution rate increases, with an average loss of about 5 % at 100 % of the substitution rate [21,34]. Moreover, the LS-NCA mix with the highest wet density already exhibited the highest SR, suggesting that the SR of the mix has a significant influence on density-driven segregation. In other words, in the highest SR mix, the bottom layer of the specimens contains a higher concentration of coarse aggregates, which are denser than the cement paste layer formed at the surface [78,79]. This correlated behavior is shown in Fig. 10.b.

3.3.4. Hydration heat

The hydration heat and the rate of heat evolution, with the total hydration heat for the four SCC mixes under consideration, are illustrated in Fig. 11. Across all mixes, the hydration process typically occurs in five stages: (i) pre-induction (rapid dissolution of C_3S), (ii) induction (dormant period), (iii) acceleration (rapid growth of C-S-H), (iv) deceleration, and (v) slow reaction (Fig. 11.a) [80]. During the pre-induction or dissolution period, C_3S rapidly dissolves upon wetting within seconds, but the dissolution rate quickly slows down. Two hypotheses explain the rapid decay of this dissolution rate: (i) the metastable barrier hypothesis, which suggests that a continuous but thin metastable layer forms around the C_3S particles, passivating their surface and thus restricting their access to water or limiting the diffusion of

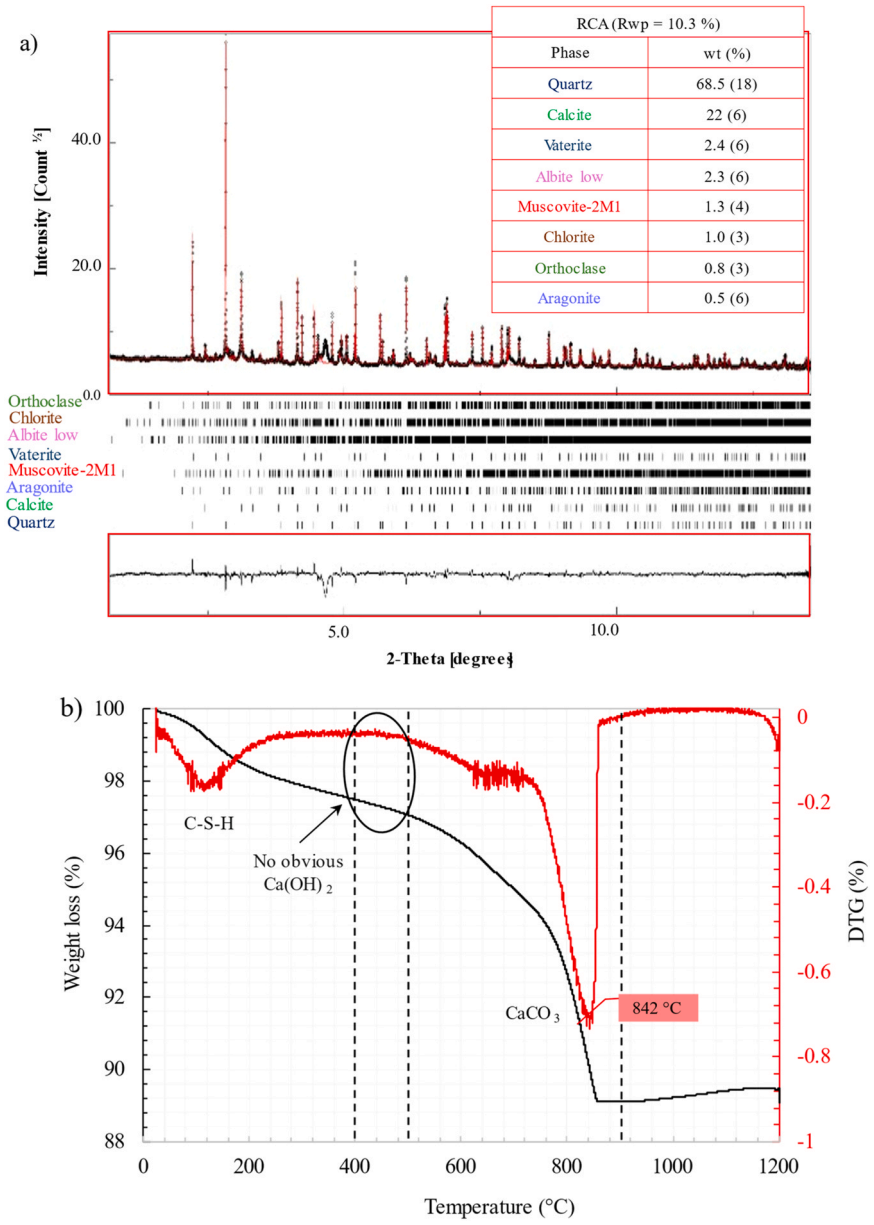

Fig. 7. a) XRD patterns showing the mineralogical composition and b) TGA/DTG curve demonstrating the hydrated phases found in the adhered old mortar of RCA.

detaching ions away from the surface; or (ii) slow dissolution step hypothesis, where the reaction slowing down is vindicated by the observed roles of crystallographic defects in the early hydration processes [81, 82]. The induction "dormant" period follows the initial dissolution of the C_3S phase and is characterized by low chemical activity [83]. The length of the induction period may indicate how long the cement-based material remains workable. The extent to which the induction period is extended or shortened is linked to several factors highlighted in [82,84]. In the case of LS-NCA, the prolonged induction period of this mix compared to other mixes can be related to its rheological instability. In other words, the bleeding and aggregate settlement observed in this mix may increase the local water availability, diluting the ion concentration and delaying the hydration in these areas [85].

Moreover, considering the differences in hydration heat , in decreasing order, of the SSP-NCA and SSP-RCA, it can be suggested that the higher water absorption of RCA during the hydration process reduces the water availability to hydrate C_3S; therefore, the growth of cement hydrates is slightly reduced. Moreover, the difference between LS-RCA and SSP-RCA may rely on the distinct filler effect of LS and SSP (Fig. 11.a). The difference remains in surface area contribution and surface properties of the employed fillers. The additional surface area SSP compared to LS is expected to offer additional nucleation sites for the heterogeneous formation and growth of early-age hydration products [80]. Nevertheless, the presence of organic matter in SSP may partially block these sites, thereby impeding the cement hydration reactions [30]. The intracrystalline organic matrix of SSP consists of polysaccharides, such as chitin, proteins, and glycoproteins, all of which are rich in amino acids with carboxyl (-COOH) functional groups [86–88]. In the alkaline pore solution, these organics progressively decompose, releasing oxygenated functional groups that create negatively charged sites with a strong affinity for Ca^{2+} (C_3S) and Al^{3+} (C_3A) [89,90]. The chelation of Ca^{2+} and binding of Al^{3+} reduce their availability in the reaction medium, thereby disturbing early hydration reactions, including ettringite formation, and slowing the nucleation rate of C-S-H [91]. Moreover, complexation through these active oxygenated groups can lead to adsorption onto reactive surfaces, blocking active sites for the nucleation and growth of hydration products [92]. Furthermore, during the acceleration stage, C_3S and a small amount of

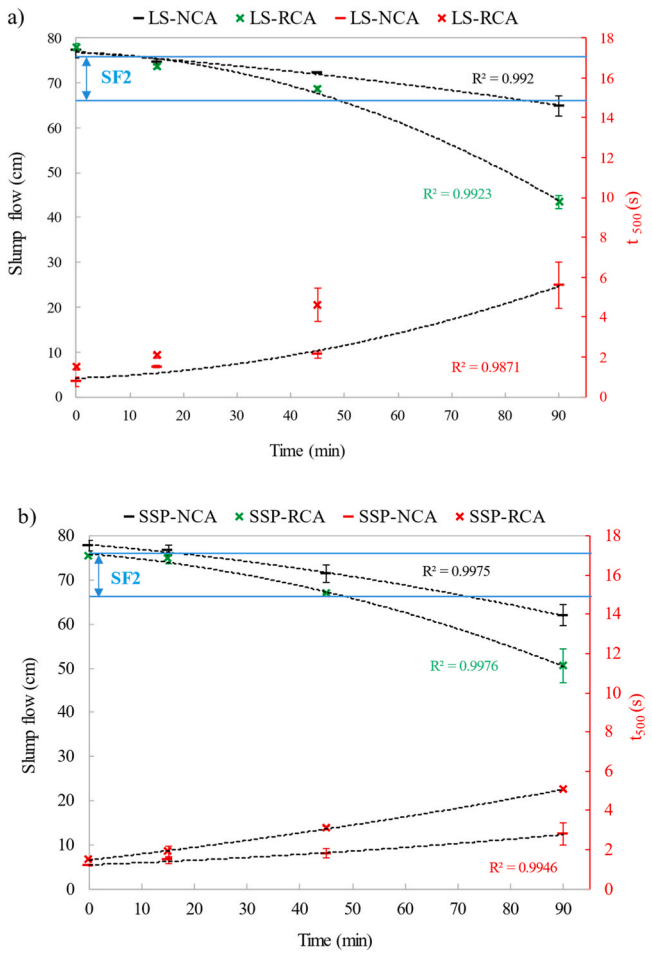

Fig. 8. Slump flow and T_{500} values of (a) LS-based SCC mixes and (b) SSP-based SCC mixes.

Table 6
VSI of the four SCC fresh mixes.

SCC	VSI operator 1	VSI operator 2	VIS average	SCC stability
LS-NCA	2	2	2	Stable (S) to unstable (US)
LS-RCA	1	1.3	1.15	S
SSP-NCA	1	0.7	0.85	S to highly stable (HS)
SSP-RCA	0.5	0	0.25	HS

(β-)dicalcium silicate (β-C_2S) dissolution accelerate, thereby increasing the rate of C-S-H growth. Concurrently, the Ca^{2+} and hydroxide ion (OH^-) concentration steadily rises within the water solution until the Ca $(OH)_2$ precipitation begins [93]. The LS-RCA, SSP-NCA, and SSP-RCA mixes show nearly the same hydration heat, which can also be seen in (Fig. 11.a), which aligns with trends previously reported in comparable systems [58,80,94–97]. These mixes exhibit the highest exothermic peak, peaking at approximately 49 $J.g^{-1}.h^{-1}$, 51 $J.g^{-1}.h^{-1}$, and 43 $J.g^{-1}.h^{-1}$, respectively (Fig. 11.b). The corresponding peaks, which correspond to the exothermic hydration of C_3S and C_2S, are narrow and occur within a similar time range, around 5 h. In contrast, LS-NCA shows the lowest exothermic peak, approximately 25 $J{\cdot}g^{-1}{\cdot}h^{-1}$, and the appearance of this exothermic peak shifted to 10 h. This suggests that LS-NCA has the lowest C-S-H growth among the mixes, which is inconsistent with findings reported in other studies [94,97], likely due to the reasons previously discussed.

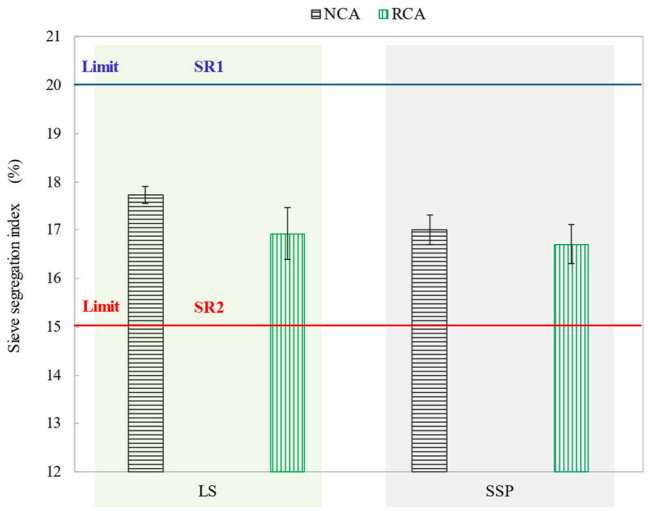

Fig. 9. Sieve segregation index of SCC mixes.

During the decelerating stage, none of the mixes exhibited a discernible shoulder peak within the 18–42 h. The considered peak would typically indicate the ettringite conversion into monosulfate. The absence of this peak is linked to the stabilizing effect of calcite on ettringite and the subsequent formation of Hc and Mc (AFm phases) (Fig. 11.a) [94,99]. However, the semi adiabatic test is not sensitive enough to confirm whether these transformations are actually occurring.

Regarding the total hydration heat release, LS-NCA exhibits a sensibly comparable cumulative heat release to the other mixes by the end of 75 h, with values ranging between 229 $J{\cdot}g^{-1}$ and 241 $J{\cdot}g^{-1}$. This may indicate that despite its delayed and lower peak heat release rate, it eventually reaches a comparable degree of hydration (Fig. 11.b).

3.4. Hardened properties

3.4.1. Compressive strength

The time evolution of the compressive strength for the cubic specimens of SCC mixes is given in Fig. 12.a. Although the delayed hydration rate and the high SR of LS-NCA, the latter exhibits around 8 % larger compressive strength than SSP-NCA on the first day of water curing. The higher compressive strength of LS-NCA may be attributed to the favorable curing conditions, which likely mitigated excessive water evaporation caused by higher bleeding during the in-mold curing. The water curing compensates for this moisture loss and supports the mix's strength development. Additionally, the crystalline structure of LS and its surface properties positively impact the early-age compressive strength of concrete with no significant effect in later stages compared with SSP (§ 3.1.1), consistently with the semi-adiabatic calorimetry results. After 7 days, the compressive strength development is more significant with the SSP-NCA, with around 34 % increase in compressive strength, 13 % higher than the increase observed for LS-NCA. The difference in the compressive strength gain can be attributed to SSP's distinct particle characteristics, suggesting that the SSP's rough surface, porous grains, and higher packing density enhance the interparticle cohesion and facilitate better mechanical interlocking [100–102], with the continuous refinement of the pore structure with the carboaluminates phases, potentially improving the interfacial transition zone (ITZ). After 28 days, the two mixes reached the same compressive strength of 40 MPa. As reported in [103], the 28-day compressive strengths of SCC are dominated mainly by the binder composition over water/binder ratio as in conventional workability concrete. However, over 28 days, the LS mixes continue to gain compressive strength, whereas the SSP mixes exhibit a moderate decline in compressive strength, which is not a

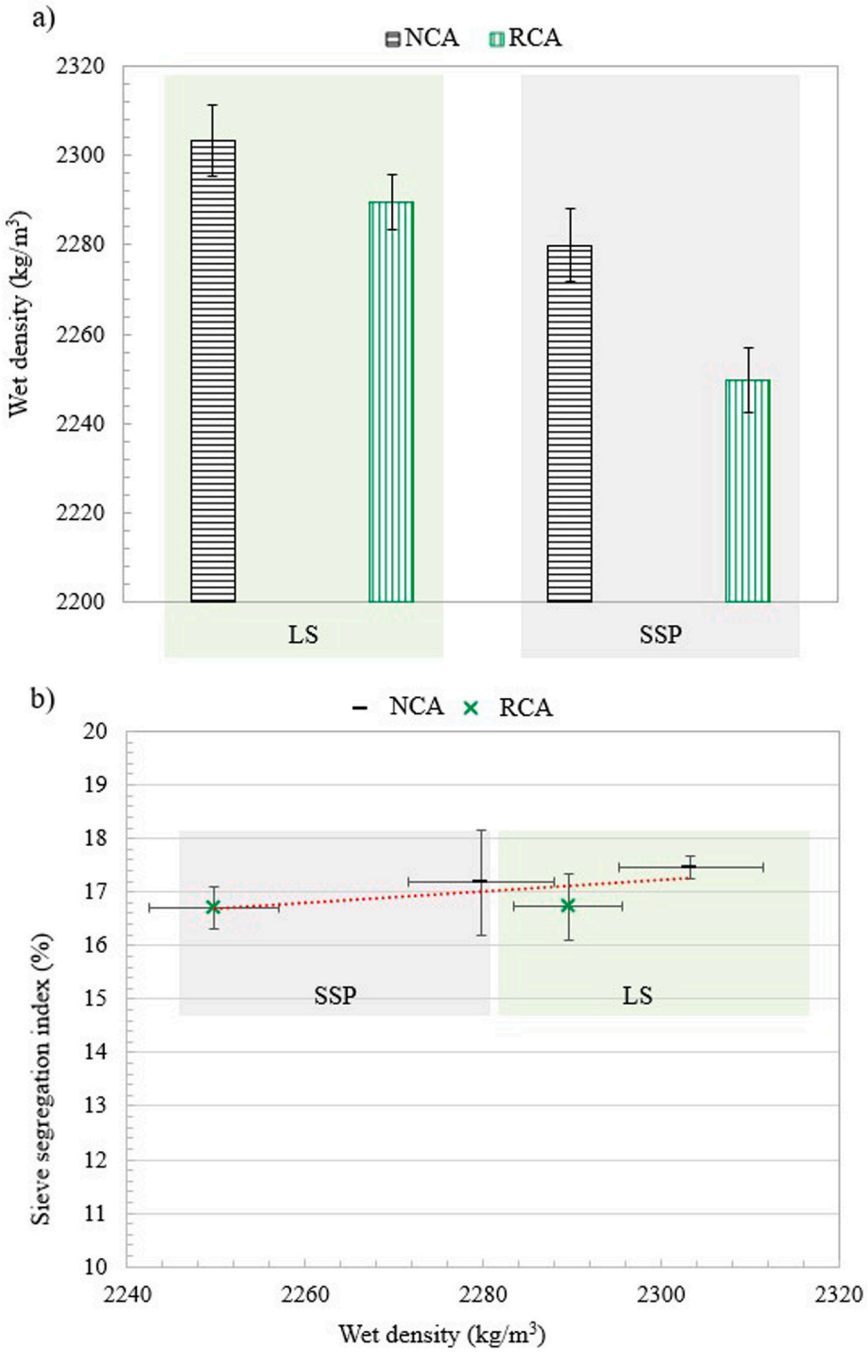

Fig. 10. a) Wet density of SCC mixes and b) relationship between SR and wet density.

typical trend reported in other studies [57,104]. Two factors can be the sole cause of the observed decrease in compressive strength: (i) the dilution effect of SSP [105,106], and (ii) the organic impurities in the SSP, which cause it to react chemically differently compared to purely mineral $CaCO_3$, as previously discussed in § 3.2.4. While this latter effect may not be particularly detrimental during the first 28 days of curing, it becomes more evident at later ages (90 days). The perturbation of the hydration process by organic matter may lead to delayed ettringite precipitation (DEF) and even late-stage C-S-H growth within the microstructure, which can generate internal stresses and promote the extension of microcracks [107–109], consistent with MIP results, ultimately lowering the long-term compressive strength of the concrete [91, 110,111]. Nevertheless, it is interesting to note that the RCA mixes exhibit a compressive strength lower than that of the mixes with NCA. The compressive strengths of LS-RCA and SSP-RCA converge throughout the curing ages and follow the same increasing trend until the 28th day of curing. At this age, LS-RCA and SSP-RCA showed moderate strength reductions of approximately 8 % and 11 %, respectively, relative to their NCA SCC counterparts. These results are consistent with those previously reported in the literature [112,113] and represent a significantly lower strength loss compared to values reported in other studies [114, 115]. The slight compressive strength loss is mainly due to the RCA's higher water absorption capacity and lower mechanical properties (§ 2.1.2). However, the limited compressive strength loss can be attributed to the surface roughness of RCA, the high fine content, the dried state of RCA, and the water compensation method used in the SCC formulation [18,116]. After 90 days of curing, while the compressive strength gap between LS-RCA and LS-NCA remains approximately the same, it

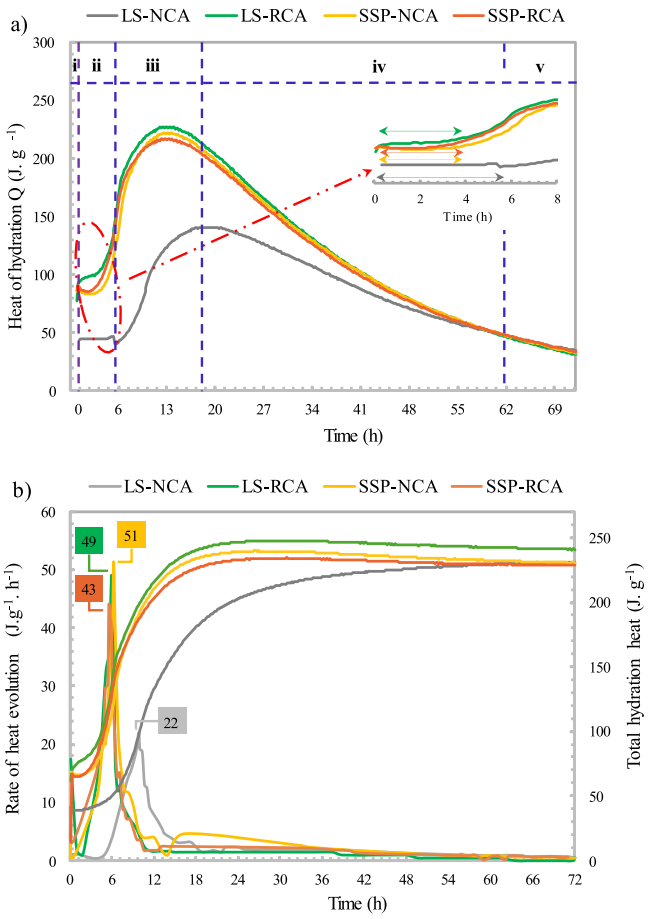

Fig. 11. Semi-adiabatic test results: a) hydration heat and b) the rate of hydration evolution and the total hydration heat.

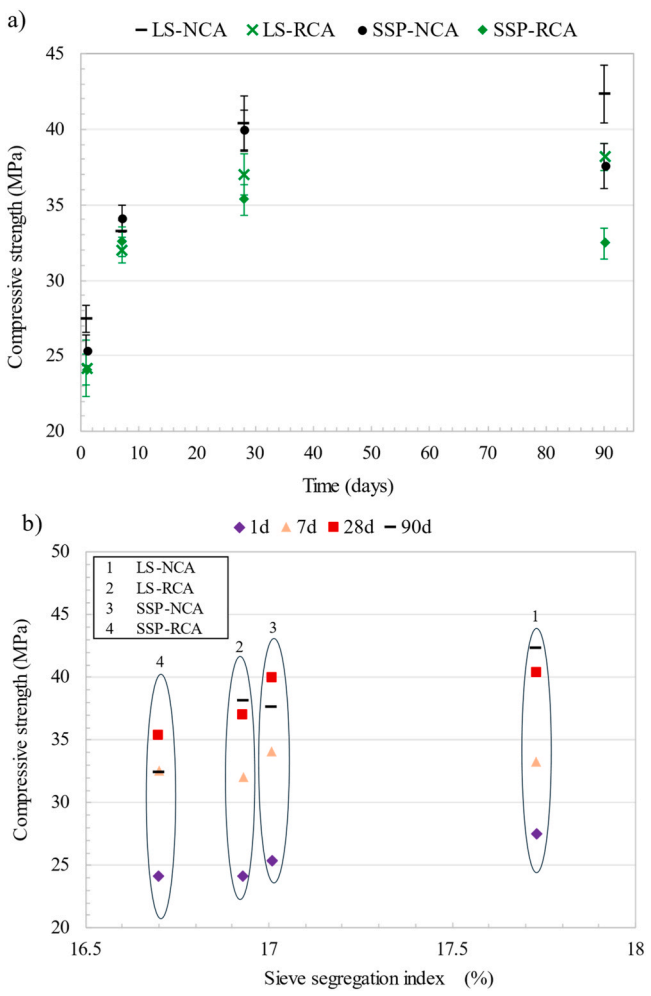

Fig. 12. a) SCC mixes compressive strength and b) relationship between SR and compressive strength.

increases to around 14 % between SSP-RCA and SSP-NCA.

Furthermore, despite the differences in SR observed across all SCC mixes, the compressive strength remains unaffected, particularly remarkable in the LS-NCA mix, which exhibits the highest segregation resistance and compressive strength at early ages. Overall, the compressive strength develops consistently across all curing ages without being significantly influenced by variations in SR (Fig. 12.b) [117,118].

3.4.2. *Bulk density, porosity accessible to water, and water absorption*

The overall bulk density evolution of the mixes (Fig. 13 a and b) follows the same trend as the ones observed for compressive strength. As the hydration process proceeds, the hydration products enhance the packing density of the SCC, thereby enhancing the bond with the cementitious matrix and the other aggregates. This trend is particularly evident in the LS mixes, which exhibit a continuous increase in bulk density throughout the 90 days of curing (Fig. 13.a). As indicated by Wu et al. [119], an optimum amount of LS maximizes the packing, thus leading to tighter spacing and more densely packed C-S-H gel within the ITZ. Conversely, the SSP mixes demonstrate a comparable density to LS and follow a similar increasing trend up to 28 days. Beyond this age of curing, their density decreases up to 90 days of curing (Fig. 13.b). First, the higher density of LS mixes, whether with NCA or RCA, compared to SSP mixes, is probably due to the LS density being slightly higher than that of SSP (§ 2.1.1). Second, the density loss for SSP mixes may indicate potential changes within their microstructure. One potential explanation still relies in the alteration of the molecular binders between calcite crystals of the shell fragments (§3.3.1). Furthermore, regardless of the SCM used, the SCC mixes containing RCA demonstrate a lower density than their counterparts with NCA, explaining partly their lower compressive strengths. The lower density, therefore, is attributed to the lower bulk-specific density of RCA [120]. These findings are consistent with [121,122].

Among the NCA mixes, the LS mix exhibits a slightly higher porosity than the SSP mix (Fig. 13.c and.d). The difference in porosity noticed during the 28 days of curing may be attributed to the combined effect of the finer particle size distribution of SSP and the rheological properties of the SSC produced with LS (§ 3.2.2). Moreover, while the SSP mix demonstrates no further significant reduction after 28 days, the LS mix continues to exhibit a gradual decrease in porosity until 90 days of curing. The observed trends highlight the close connection between porosity accessible to water, compressive strength, and bulk density. Regarding the mixes containing RCA, they demonstrated higher porosity compared to their counterparts with NCA, aligning with previous studies [72,123].It is well documented that the incorporation of RCA in all types of concrete results in the formation of two new ITZ, one between the old and the new mortar and another between the surface of the aged NCA and the new mortar. Conversely, a single ITZ forms within the concretes containing NCA. The porosity and the thickness of these ITZ govern the mechanical behavior, and a part of the porosity level and the water absorption capacity of the concrete. Therefore, the difference in the porosity between the mixes containing the RCA lies in the respective effects and physicochemical properties of LS and SSP [124,125].

The variation in the porosity accessible to water in a specific mix directly affects its water absorption capacity by either providing or

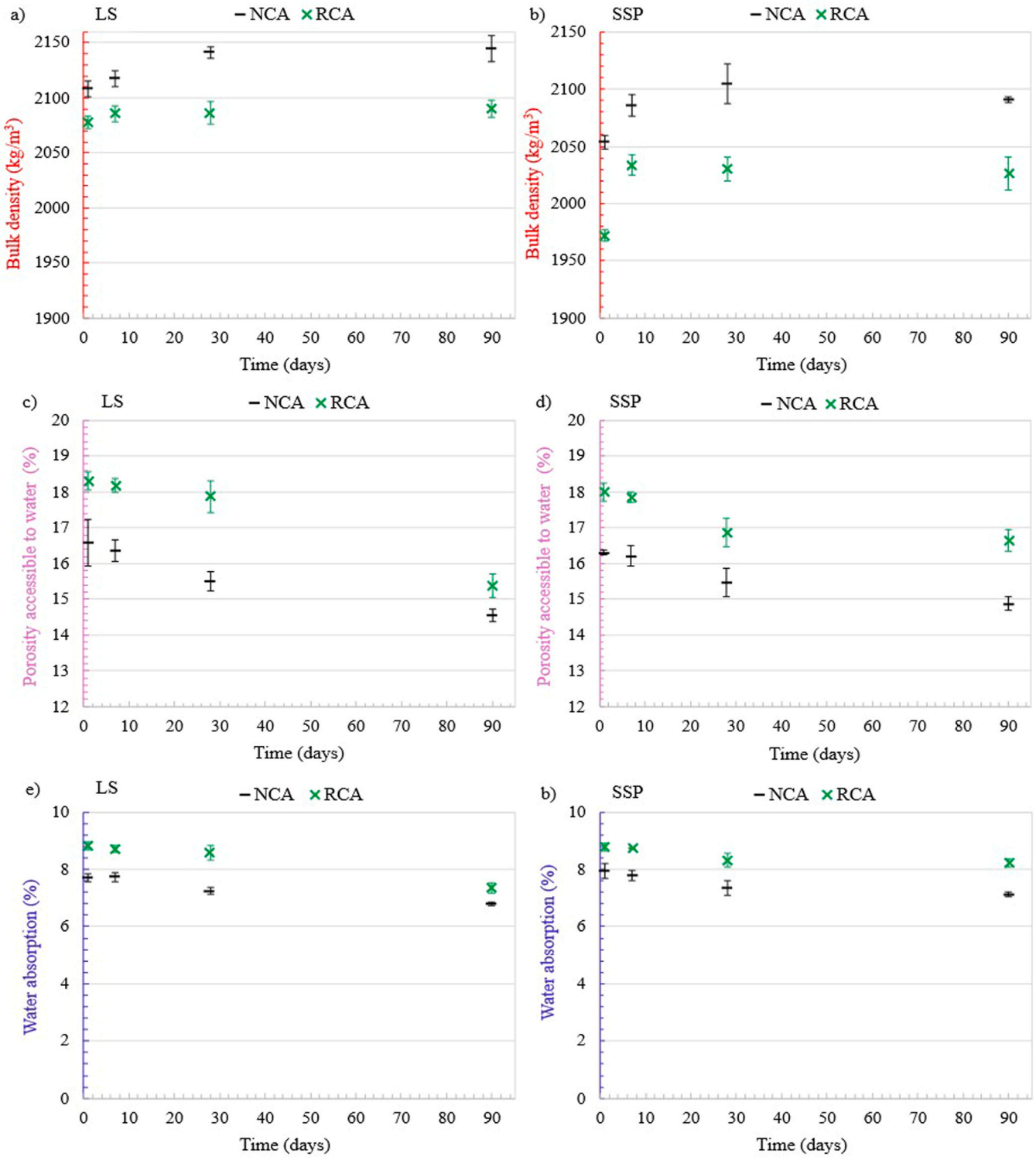

Fig. 13. Physical properties of a), c), e) LS-NCA and LS-RCA, b), d), f) SSP-NCA and SSP-RCA.

restricting pathways for water infiltration into the concrete matrix [126, 127]. Therefore, the evolution of the water absorption capacity of all mixes (Fig. 13.e and f) is a result of porosity changes occurring within their matrix, which, in turn, can be linked to the physicochemical properties of the precursor used and the rheological behavior of each mix. It has been reported, for instance, that SSP leads to a highly porous ITZ and introduces a large volume of macropores, primarily caused by air entrapped by proteins present in the organic matrix, which consequently increases water absorption [110,128,129]. Moreover, under the highly alkaline pore solution of concrete, the organics are prone to dissolution or denaturation, similarly contributing to the alteration of these properties [130].

3.5. *Microstructural analysis*

3.5.1. *Thermogravimetric analysis*

Fig. 14 presents the TGA/DTG curves, illustrating the hydration progress of the SCC mixes. Three main mass loss events can be observed

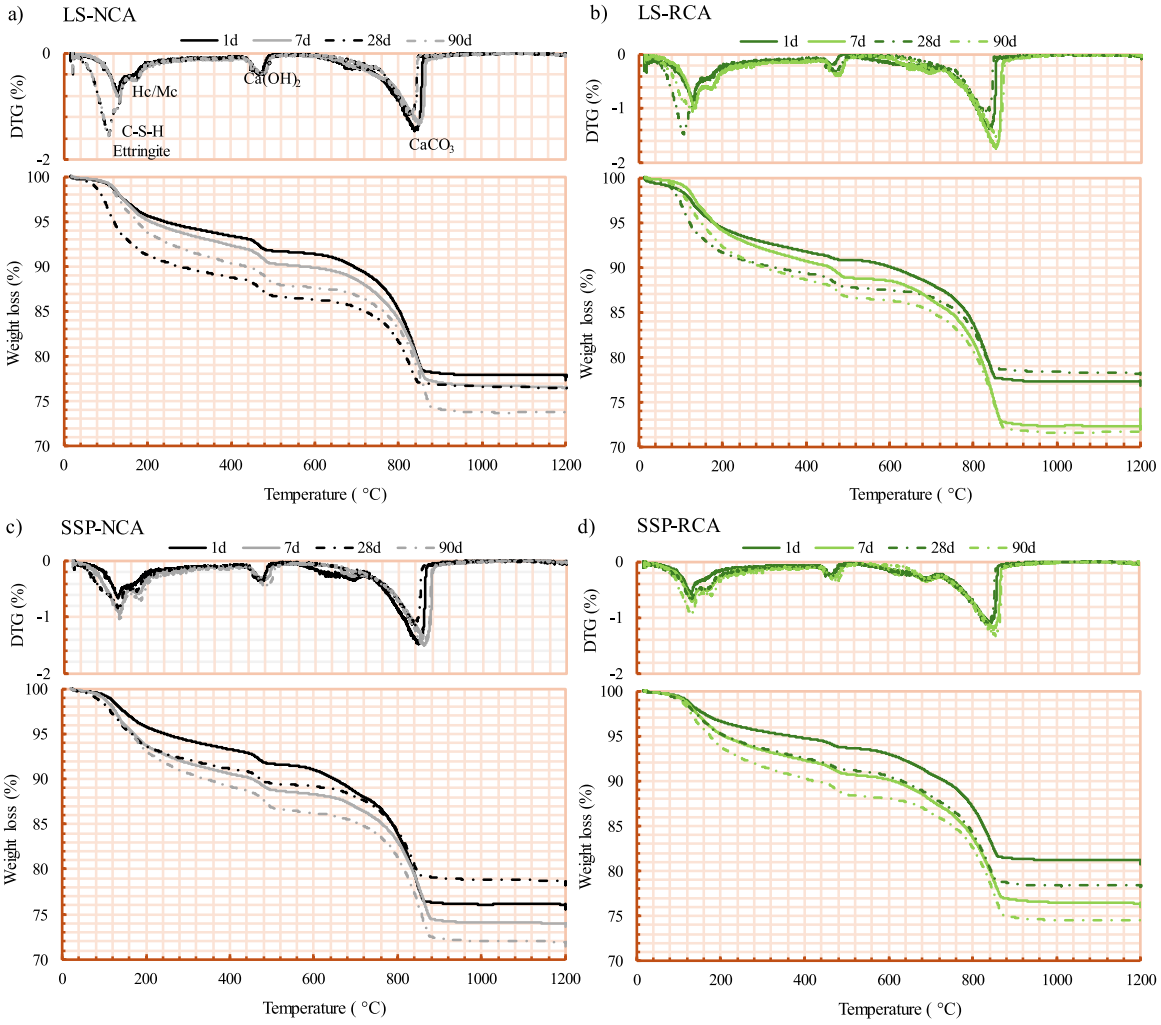

Fig. 14. TGA/DTG curves of a) and b) LS-based SCC mixes, and c) and d) SSP-based SCC mixes over different curing ages.

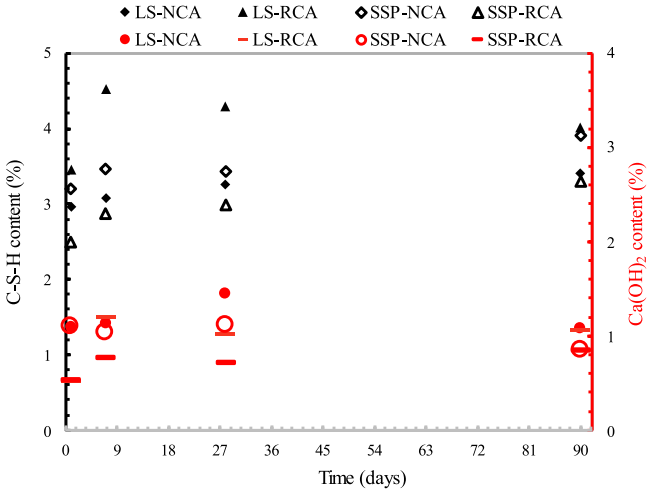

Fig. 15. C-S-H (black symbols) and $Ca(OH)_2$ (red) contents in the mixes as integrated from TGA/DTG curves.

across all SCC mixes' TGA curves: C-S-H dehydration, $Ca(OH)_2$ dihydroxylation within the temperature ranges mentioned earlier (§ 2.4.4), and the decarbonation of $CaCO_3$ occurring between 700 °C and 900 °C [14]. These curves exhibit a characteristic profile consistent with those documented in previous studies [58,131]. The $CaCO_3$ content primarily originates from the LS and SSP in the SCC mixes rather than from natural carbonation. Moreover, a simple look into the DTG curves reveals that a small endothermic peak appears within the dehydration range of C-S-H, appearing within the range of 170–180 °C in our samples. This peak indicates Hc/Mc decomposition, supporting the claim that including SSP and LS in the SCC mixes promotes the formation of these phases [132]. However, it is difficult to detect this reaction in the TGA curves, as they show only a subtle slope change.

The evolution of hydrate and hydroxyl contents in SCC mixes for the various water curing ages is evaluated through integration of the DTG curves in the C-S-H and $Ca(OH)_2$ ranges (Fig. 15). It is well known that the hydration products fill the pores, densify the cementitious matrix microstructure, and ensure the inter-particle binding, with C-S-H being the primary hydrate responsible for concrete's strength. Comparing the C-S-H content in LS-NCA and SSP-NCA, both mixes show similar levels during 28 days of water curing, with slightly higher content observed in SSP-NCA, particularly at 7 days. This suggests that the hydration of LS-NCA may be slightly delayed at early ages, possibly due to its rheological properties. Larger porosity in SSP can also contribute to this behavior. At 90 days, while LS-NCA shows stable C-S-H formation, SSP-NCA continues to develop more C-S-H compared to what was observed at 28 days. Nevertheless, a decline in compressive strength was observed for SSP-NCA at this age. As will be discussed later, SEM observations reveal poorly hydrated C-S-H within the SSP-NCA matrix. The poorly formed C-S-H compromises the matrix densification and weakens the intrinsic

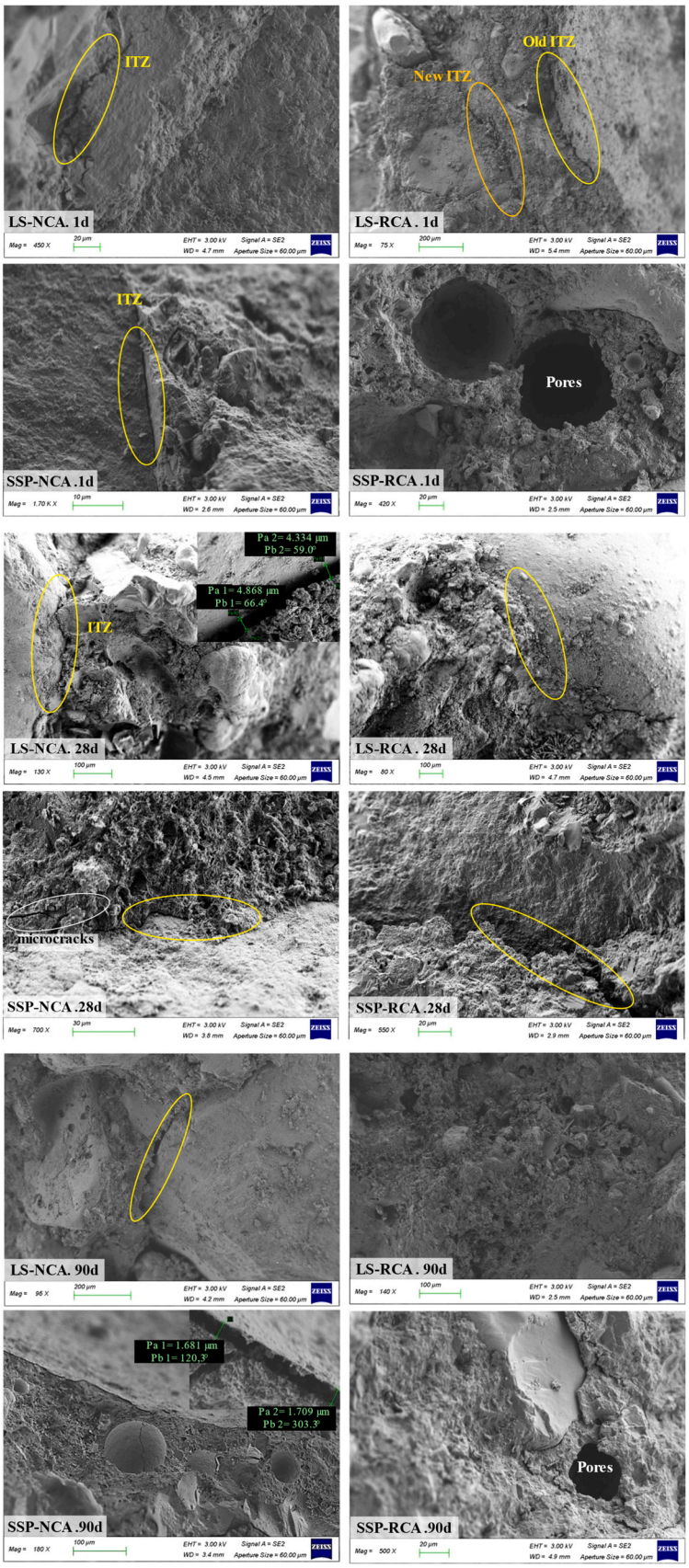

Fig. 16. SEM images on top of ITZ of SCC mixes.

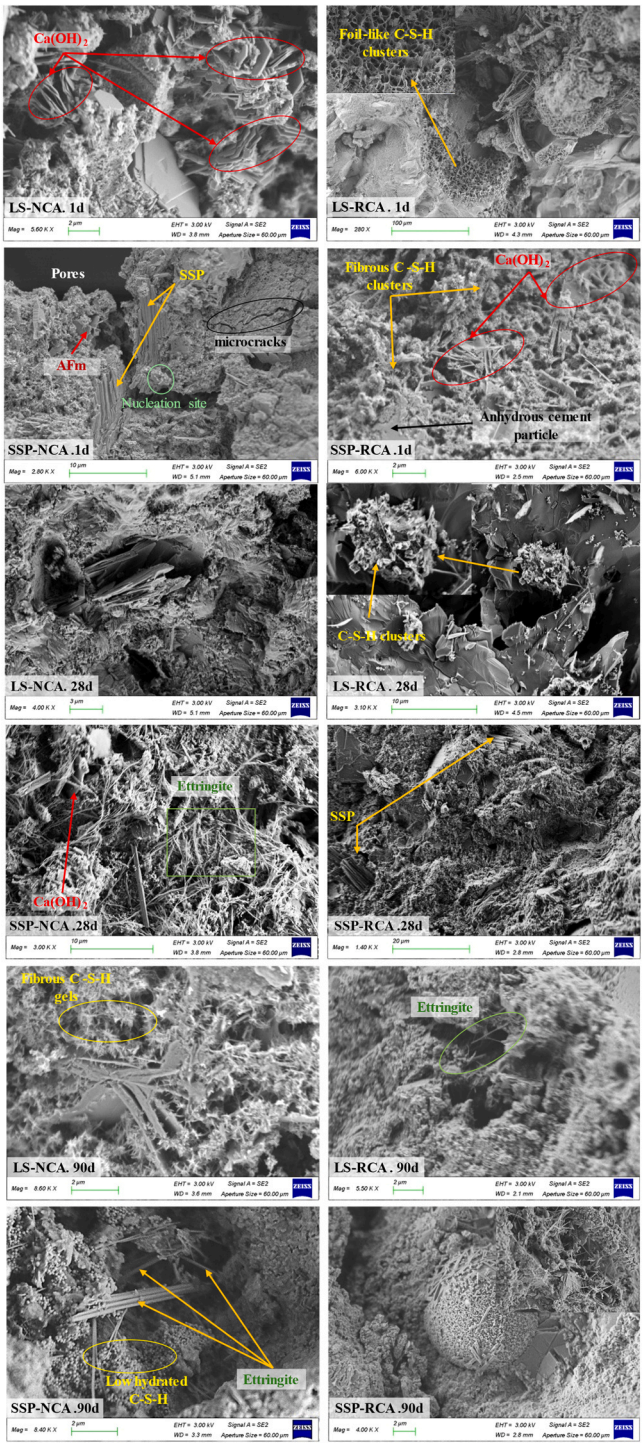

Fig. 17. SEM images of the mortar matrix evolution of SCC mixes.

cohesive capacity of the phase [133]. Moreover, it is more susceptible to the initiation of microcracks at its interfaces, further contributing to the observed reduction in compressive strength [134,135]. Comparing the mixes with RCA, LS-RCA exhibits the highest amount of C-S-H among all other mixes, contrary to SSP-RCA, which displays the lowest amount of C-S-H across all ages of water curing. These findings are consistent with the pore refinement trends observed through MIP testing. It is worth mentioning that it is difficult to attribute the measured C-S-H content in these mixes entirely to ongoing hydration, as the old mortar adhering to the RCA surface already contains pre-existing C-S-H. This may lead to an overestimation of the actual extent of hydration.

3.5.2. *Microstructural observations*

The SEM images of our samples (Fig. 16) reveal that the aggregates are well-embedded in the mortar matrix, with a few 20–60 μm diameters macropores. A noticeable reduction in ITZ thickness is observed across all SCC mixes over time. For instance, the ITZ thickness in LS-NCA is approximately 5 μm in width at 28 days, and around 2 μm at 90 days in SSP-NCA. These values are significantly lower than those typically observed in normal concretes, where ITZ thickness ranges from 9 μm to 51 μm [136]. One explanation for this observation can be the absence of vibration during the confection of SCC that reduces the amount of water accumulating around the aggregates, thereby reducing the ITZ thickness [137].

The microstructure of the mortar matrix in the SCC mixes is also revealed in the SEM images illustrated in Fig. 17. At the early stage of hydration (1 day), the cement particles across all SCC mixes are not yet fully hydrated, and the nucleation and growth of hydration products on SSP and LS surfaces remain incomplete. Pores, microcracks, and are also evident within the mortar matrix of all four SCC mixes. Notably, the C-S-H formed in the LS-RCA mix exhibits a foil-like morphology, whereas in the other mixes, it appears fibrillar. The foil-like structure is commonly associated with cement matrices containing a high content of SCM. As Richardson also states, the foil-like C-S-H morphology is more efficient at filling space, leaving no interconnected capillary pores compared to the fibrillar morphology, thereby enhancing the durability of the system [138]. Further water curing (up to 28 days) gives rise to more hydration products. However, the extent of hydration within each mix remains difficult to assess visually. In the SSP-NCA mix, ettringite growth appears random, chaotic, and interspersed among other hydration products. By 90 days, ettringite morphology becomes more uniform and consistent in size across all mixes. Nonetheless, the LS-NCA and LS-RCA matrices exhibit more advanced hydration, as evidenced by a denser microstructure and more developed C-S-H phases. In contrast, the SSP-RCA and SSP-NCA mixes display less hydration, as low-hydrated C-S-H appears in their matrices, explaining the observed decline in compressive strength at this age of curing (§ 3.3.1). The identification of hydration products formed in the studied SCC mixes was guided by morphological characteristics reported in [139–141].

3.5.3. *Pore structure analysis: MIP testing*

The results of mercury porosimetry analyses carried out at curing times of 1 and 28 days for the four SCC mixtures are shown in Fig. 18. The pore system in SCC or concrete usually comprises four types of pores. The first type is the gel pores, which are micropores with a dimension ranging from 0.5–10 nm and occupied with C-S-H [142]. The second type is the capillary pores. These pores are mesopores with an average radius of 5–5000 nm [143]. Pores of the third type are macropores generated by deliberately entrained air, and the fourth type is also made of macropores, but resulting from inadequate concrete compaction [144]. Pores with a diameter below 20 nm are considered harmless to concrete strength but are directly responsible for its creep and shrinkage, specifically the smallest gel pores in the 1.5–2.0 nm range. Pores with diameters within the 20 nm–50 nm and 50 nm–200 nm ranges, and those above 200 nm can be minimally to significantly harmful [145]. After one day of curing, the LS-NCA mix exhibits a lower total porosity than SSP-NCA, and both mixes demonstrate reduced porosity relative to their respective counterparts with RCA. As curing progresses, a general decreasing trend of 1–3 % in total porosity is observed across all mixes, with the relative differences between them remaining consistent over time (Fig. 18.a and d). These patterns are consistent with those observed in water-accessible porosity, except that the LS-NCA and SSP-NCA display comparable porosity values at 1 day of curing. The progressive reduction in porosity over time is primarily attributed to the continued formation of hydration products, which fill and refine the capillary pore structure by reducing pore diameters (Fig. 18.b and e). Further, the pore size distribution (Fig. 18.c and f) indicates that at one day of curing, the pore system of LS-NCA comprises

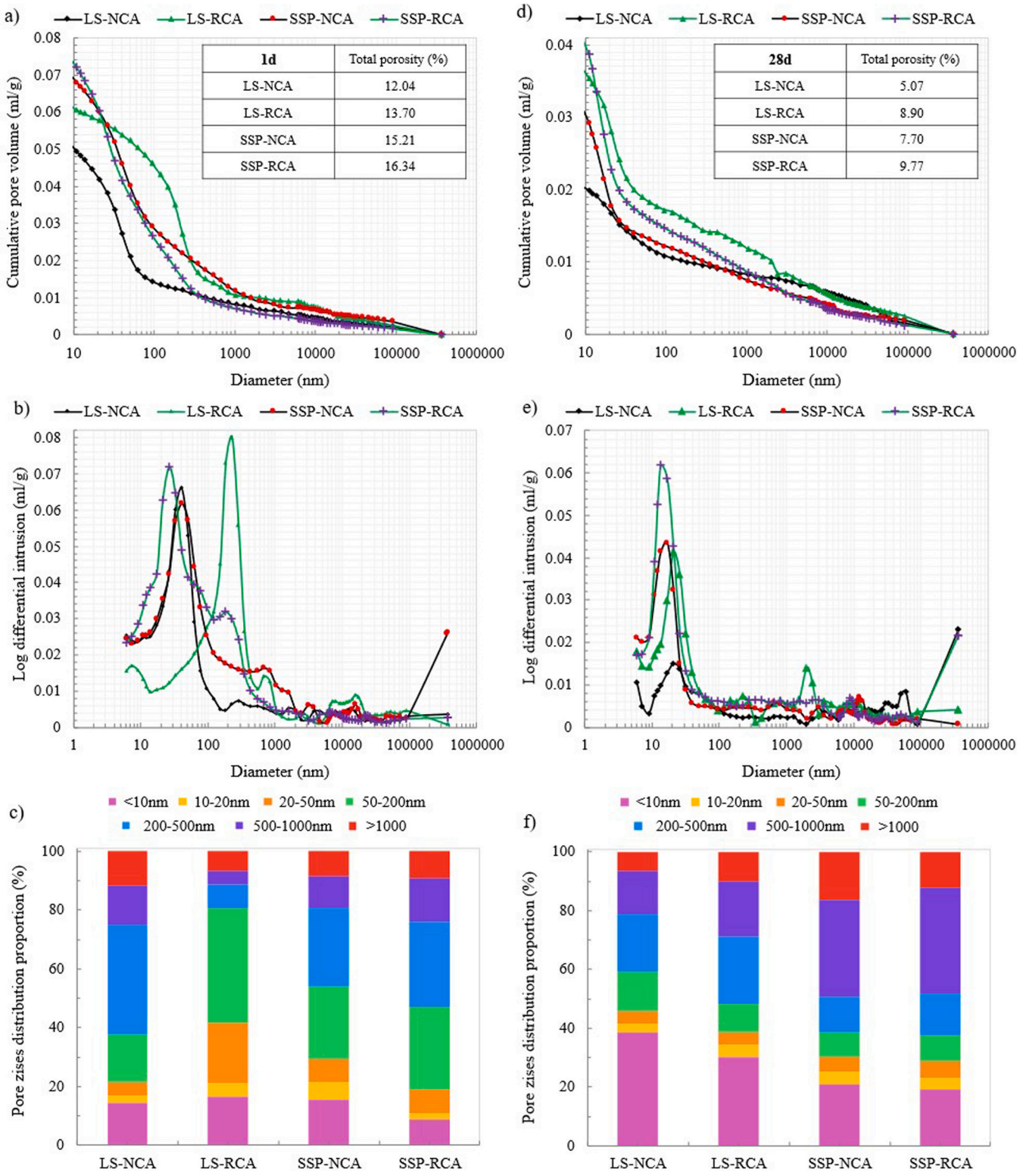

Fig. 18. Pore system of SCC mixes at 1 day (a-c) and 28 days (d-f) of curing.

approximately 60 % of pores with diameters larger than 200 nm, in contrast to 20 % in LS-RCA, 46 % in SSP-NCA, and 53 % in SSP-RCA. After 28 days of curing, both LS-NCA and LS-RCA exhibit a substantial increase in hardness, corresponding to a reduction in the total fraction of harmful pores, consistent with previously observed trends [131]. This observation suggests a more refined pore structure in these mixes, attributed to enhanced hydration kinetics. However, SSP-NCA and SSP-RCA demonstrate a notable development of harmful pores (>500 nm) at 28 days, a phenomenon previously reported in the literature [146], supporting the earlier suggestion of (DEF), which could explain the decline in compressive strength observed at 90 and the changes in the physical properties of these mixes (§ 3.3.1 and § 3.3.2).

4. Conclusions

This study aimed to investigate the combined effect of SSP and 100 % RCA on the fresh properties of SCC and the evolution of its hardened properties over the 90 days of curing. Our analysis of the experimental results led to the following main conclusions:

- **Rheological properties**: Evaluating the fresh properties of the four SCC mixes reveals distinct behaviors between SSP and LS. SSP proves to be more beneficial for the rheological properties of SCC in terms of stability to segregation and plastic viscosity, despite the slight reduction in slump flow. Regarding the use of RCA, their high absorption capacity, although not favorable for long-term workability retention, resulted in slump flow values comparable to those of NCA during the first 15 min, due to the drying and water compensation. Nevertheless, RCA enhanced the cohesion of SCC, reduced bleeding, and improved resistance to both static and dynamic segregation.
- **Hydration kinetics:** The semi-adiabatic calorimetry results revealed a delayed onset of hydration in the LS-NCA mix during the initial stage. Meanwhile, the other mixes exhibited similar hydration kinetics.
- **Compressive strength:** The incorporation of RCA resulted in moderate reductions in strength of approximately 8 % (for LS-RCA) and 11 % (for SSP-RCA), respectively, compared to mixtures containing NCA. On the other hand, SSP mixes demonstrated higher compressive strength development at mid ages, but this trend reversed beyond 28 days, with a reduction in strength at 90 days. These trends were observed in water accessibility and bulk density and are most probably due to the organic content of natural biominerals of the SSP, which interfered with the hydration reactions and consequently affected the pore distribution.
- **Microstructure properties:** The MIP results at 28 days revealed that the pore system of SSP mixes developed a higher proportion of harmful pores (>500 nm) than LS mixes, explaining the differences in the measured compressive strength. The refinement extent of each mix correlates with the hydrate formation content proportion through TGA and the microstructure development through SEM.

These conclusions highlight the potential of using SSP and RCA as sustainable alternatives in SCC mix design, emphasizing the importance of understanding their effects on both fresh and hardened properties to achieve reliable SCC performance characteristics. In line with previous findings on LS-based systems, the SCC developed in this study can likewise be considered for structural precast elements, as it is classified within strength class 25/30 in accordance with NF EN 206 +A2/CN [147]. Nevertheless, the decline in compressive strength observed at 90 days for SSP-based specimens warrants further investigation.

CRediT authorship contribution statement

Daniel Chateigner: Writing – review & editing, Visualization, Validation, Supervision. **Stéphanie Gascoin:** Visualization, Validation. **EL Moustapha Bouha:** Writing – review & editing, Visualization, Validation, Supervision. **Fouzia Khadraoui:** Visualization, Validation, Supervision. **GUESSOUM Meriem:** Writing – review & editing, Writing – original draft, Methodology, Investigation, Formal analysis, Conceptualization. **Walid Maherzi:** Writing – review & editing, Visualization, Validation.

Declaration of Competing Interest

The authors declare that they have no known competing financial interests or personal relationships that could have appeared to influence the work reported in this paper.

Acknowledgements

BUILDERS Ecole d'ingenieurs actively participates in the various themes of sustainable development and societal responsibility that are addressed, in particular in the 17 Sustainable Development Goals (SDGs). Our teacher-researchers, staff and students are pro-active contributors to all the SDGs. This scientific article contributes to the objectives of SDGs number 12 and 13. We acknowledge the European Synchrotron Radiation Facility (ESRF) for provision of synchrotron radiation facilities and Momentum Transfer for facilitating the measurements. Jakub Drnec is thanked for assistance and support in using beamline ID31. The measurement setup was developed with funding from the European Union's Horizon 2020 research and innovation program under the STREAMLINE project (grant agreement ID 870313). Measurements performed as part of the MatScatNet project were supported by OSCARS through the European Commission's Horizon Europe Research and Innovation programme under grant agreement No. 101129751.

Data availability

No data was used for the research described in the article.

References

[1] Our World in Data, Cumulative CO_2 emissions from cement, ⟨Https://Ourworldindata.Org/⟩ (Accessed 22.07.24). (2022). ⟨https://ourworldindata.org/⟩ (accessed July 22, 2024).
[2] MineralInfo, Careers in France, ⟨Https://Www.Mineralinfo.Fr/Fr/Ressources-Minerales-France-Gestion/Carrieres-France⟩ (2020).
[3] A. Diemer, C.E. Nedelciu, M.E. Morales, C. Batisse, C. Cantuarias-Villessuzanne, Waste management and circular economy in the French building and construction sector, Front. Sustain. 3 (2022), https://doi.org/10.3389/frsus.2022.840091.
[4] R. Fernández-Penas, C. Verdugo-Escamilla, C. Triunfo, S. Gärtner, A. D'Urso, F. Oltolina, A. Follenzi, G. Maoloni, H. Cölfen, G. Falini, J. Gómez-Morales, A sustainable one-pot method to transform seashell waste calcium carbonate to osteoinductive hydroxyapatite micro-nanoparticles, J. Mater. Chem. B 11 (2023) 7766–7777, https://doi.org/10.1039/D3TB00856H.
[5] B. De Pascale, G. Tarsi, P. Tataranni, C. Sangiorgi, Potential application of waste bivalve shells as recycled filler in porous asphalt concrete through rheo-mechanical analysis, Resour. Conserv Recycl 209 (2024) 107830, https://doi.org/10.1016/j.resconrec.2024.107830.
[6] M. Zelloufi, V. Ramos, B. El Haddaji, A. Bourguiba, G.K. Rollinson, J. Andersen, N. Sebaibi, M. Boutouil, Bio-colonisation, durability, and microstructural analysis of concrete incorporating magnetite and oyster shell waste aggregates in marine environment, Constr. Build. Mater. 456 (2024) 139269, https://doi.org/10.1016/J.CONBUILDMAT.2024.139269.
[7] M. Zelloufi, V. Ramos, B. El Haddaji, A. Bourguiba, S. Broom-Fendley, G. K. Rollinson, A. Guedes, J. Andersen, N. Sebaibi, M. Boutouil, Assessment of bio-colonisation, durability and microstructure of concrete exposed to intertidal and subtidal marine environments, Case Stud. Constr. Mater. 23 (2025) e05119, https://doi.org/10.1016/J.CSCM.2025.E05119.
[8] W. Xu, Y. Zhang, Y. Su, X. Zhu, L. Wang, D.C.W. Tsang, Using waste to improve the weak: recycled seashell as an ideal way to regulate the interfacial transition zone in biochar-cement composites, Constr. Build. Mater. 444 (2024) 137765, https://doi.org/10.1016/j.conbuildmat.2024.137765.
[9] G. Hondroyiannis, E. Sardianou, V. Nikou, K. Evangelinos, I. Nikolaou, Recycling rate performance and socioeconomic determinants: evidence from aggregate and regional data across european union countries, J. Clean. Prod. 434 (2024) 139877, https://doi.org/10.1016/j.jclepro.2023.139877.
[10] M. El Marzak, H. Karim Serroukh, M. Benaicha, O. Jalbaud, A. Hafidi Alaoui, Y. Burtschell, Rheological and mechanical analysis of self-compacting concrete incorporating rubber aggregates, Case Stud. Constr. Mater. 22 (2025) e04564, https://doi.org/10.1016/j.cscm.2025.e04564.
[11] Ch.R. kumar Seshagiri Rao Boddu, Self-Compacting Concrete, Imperial Journal of Interdisciplinary Research 2 (2016). ⟨http://www.onlinejournal.in⟩ (accessed March 26, 2025).
[12] M.A. Dehghani Najvani, D. Heras Murcia, E. Soliman, M.M. Reda Taha, Early-age strength and failure characteristics of 3D printable polymer concrete, Constr. Build. Mater. 394 (2023) 132119, https://doi.org/10.1016/J.CONBUILDMAT.2023.132119.
[13] Á. González-Caro, A.M. Merino-Lechuga, E. Fernández-Ledesma, J.M. Fernández-Rodríguez, J.R. Jiménez, D. Suescum-Morales, The effect of acanthocardia tuberculata shell powder as filler on the performance of Self-Compacting mortar, Materials 16 (2023) 1734, https://doi.org/10.3390/ma16041734.
[14] B. Safi, M. Saidi, A. Daoui, A. Bellal, A. Mechekak, K. Toumi, The use of seashells as a fine aggregate (by sand substitution) in self-compacting mortar (SCM),

Constr. Build. Mater. 78 (2015) 430–438, https://doi.org/10.1016/J.CONBUILDMAT.2015.01.009.
[15] T.V. Fonseca, M.A.S. dos Anjos, R.L.S. Ferreira, F.G. Branco, L. Pereira, Evaluation of self-compacting concretes produced with ternary and quaternary blends of different SCM and hydrated-lime, Constr. Build. Mater. 320 (2022) 126235, https://doi.org/10.1016/J.CONBUILDMAT.2021.126235.
[16] J. Wang, E. Liu, Upcycling waste seashells with cement: rheology and early-age properties of portland cement paste, Resour. Conserv Recycl 155 (2020) 104680, https://doi.org/10.1016/J.RESCONREC.2020.104680.
[17] P. Matar, J.J. Assaad, Concurrent effects of recycled aggregates and polypropylene fibers on workability and key strength properties of self-consolidating concrete, Constr. Build. Mater. 199 (2019) 492–500, https://doi.org/10.1016/J.CONBUILDMAT.2018.12.091.
[18] Y.-X. Liu, T.-C. Ling, K.-H. Mo, Progress in developing self-consolidating concrete (SCC) constituting recycled concrete aggregates: a review, Int. J. Miner. Metall. Mater. 28 (2021) 522–537, https://doi.org/10.1007/s12613-020-2060-x.
[19] C. Liang, H. Chen, R. Li, W. Chi, S. Wang, S. Hou, Y. Gao, P. Zhang, Effect of additional water content and adding methods on the performance of recycled aggregate concrete, Constr. Build. Mater. 423 (2024) 135868, https://doi.org/10.1016/J.CONBUILDMAT.2024.135868.
[20] V. Revilla-Cuesta, M. Skaf, A. Santamaría, J.J. Hernández-Bagaces, V. Ortega-López, Temporal flowability evolution of slag-based self-compacting concrete with recycled concrete aggregate, J. Clean. Prod. 299 (2021) 126890, https://doi.org/10.1016/J.JCLEPRO.2021.126890.
[21] R.V. Silva, J. de Brito, R.K. Dhir, Fresh-state performance of recycled aggregate concrete: a review, Constr. Build. Mater. 178 (2018) 19–31, https://doi.org/10.1016/j.conbuildmat.2018.05.149.
[22] R. Ševčík, P. Šašek, A. Viani, Physical and nanomechanical properties of the synthetic anhydrous crystalline CaCO3 polymorphs: vaterite, aragonite and calcite, J. Mater. Sci. 53 (2018), https://doi.org/10.1007/s10853-017-1884-x.
[23] M.L. Basile, C. Triunfo, S. Gärtner, S. Fermani, D. Laurenzi, G. Maoloni, M. Mazzon, C. Marzadori, A. Adamiano, M. Iafisco, D. Montroni, J. Gómez Morales, H. Cölfen, G. Falini, Stearate-Coated biogenic calcium carbonate from waste seashells: a sustainable plastic filler, ACS Omega 9 (2024) 11232–11242, https://doi.org/10.1021/acsomega.3c06186.
[24] S. Yalcın, D. Chateigner, L. Le Pluart, S. Gascoin, S. Eve, Investigation of structural and mechanical properties of BioCaCO$_3$-LDPE composites, Mater. Int. 1 (2019) 29–43, https://doi.org/10.33263/Materials12.029043.
[25] M.A. Husain, M.M. Jomaa'h, Factors affecting the compressive strength of Eco-Friendly limestone calcined clay cement (LC^3): a review, Civ. Environ. Eng. 21 (2025) 605–616, https://doi.org/10.2478/cee-2025-0046.
[26] Z. Shao, M. Cao, X. Zheng, Limestone particle sizes and sulfate impact on the early hydration of limestone calcined clay cement, J. Build. Eng. 97 (2024) 110848, https://doi.org/10.1016/j.jobe.2024.110848.
[27] S. Rode, N. Oyabu, K. Kobayashi, H. Yamada, A. Kühnle, True Atomic-Resolution imaging of (10$\bar{1}$4) calcite in aqueous solution by frequency modulation atomic force microscopy, Langmuir 25 (2009) 2850–2853, https://doi.org/10.1021/la803448v.
[28] L. Li, M. Cao, H. Yin, Comparative roles between aragonite and calcite calcium carbonate whiskers in the hydration and strength of cement paste, Cem. Concr. Compos 104 (2019) 103350, https://doi.org/10.1016/J.CEMCONCOMP.2019.103350.
[29] D. Aquilano, M. Bruno, S. Ghignone, L. Pastero, Twinning and homoepitaxy cooperation in the already rich growth morphology of $CaCO_3$ polymorphs. I. aragonite, J. Appl. Crystallogr 56 (2023) 1630–1638, https://doi.org/10.1107/S1600576723008208.
[30] S. Gowthaman, M. Chen, K. Nakashima, S. Kawasaki, Effect of scallop powder addition on MICP treatment of amorphous peat, Front Environ. Sci. 9 (2021), https://doi.org/10.3389/fenvs.2021.690376.
[31] M.E. Sosa, Y.A. Villagrán Zaccardi, C.J. Zega, A critical review of the resulting effective water-to-cement ratio of fine recycled aggregate concrete, Constr. Build. Mater. 313 (2021) 125536, https://doi.org/10.1016/J.CONBUILDMAT.2021.125536.
[32] Z.F. Akbulut, S. Guler, D. Yavuz, M.S. Avcı, Toward sustainable construction: a critical review of recycled aggregate concrete properties and future opportunities, Case Stud. Constr. Mater. 23 (2025) e05133, https://doi.org/10.1016/J.CSCM.2025.E05133.
[33] Z. Tahar, E.H. Kadri, T.-T. Ngo, A. Bouvet, A. Kaci, Influence of recycled sand and gravel on the rheological and mechanical characteristic of concrete, J. Adhes. Sci. Technol. 30 (2016) 392–411, https://doi.org/10.1080/01694243.2015.1101185.
[34] V. Revilla-Cuesta, V. Ortega-López, M. Skaf, J.M. Manso, Effect of fine recycled concrete aggregate on the mechanical behavior of self-compacting concrete, Constr. Build. Mater. 263 (2020) 120671, https://doi.org/10.1016/J.CONBUILDMAT.2020.120671.
[35] R.V. Silva, J. de Brito, R.K. Dhir, Tensile strength behaviour of recycled aggregate concrete, Constr. Build. Mater. 83 (2015) 108–118, https://doi.org/10.1016/j.conbuildmat.2015.03.034.
[36] 2009, NF EN 933-11, Tests for geometrical properties of aggregates - Part 11: Classification test for the constituents of coarse recycledaggregate.
[37] M. Guessoum, F. Boukhelf, F. Khadraoui, Full characterization of Self-Compacting concrete containing recycled aggregates and limestone, Materials 16 (2023) 5842.
[38] D. Chen, P. Zhang, T. Pan, Y. Liao, H. Zhao, Evaluation of the eco-friendly crushed waste oyster shell mortars containing supplementary cementitious materials, J. Clean. Prod. 237 (2019) 117811, https://doi.org/10.1016/J.JCLEPRO.2019.117811.
[39] F. Debieb, S. Kenai, The use of coarse and fine crushed bricks as aggregate in concrete, Constr. Build. Mater. 22 (2008) 886–893, https://doi.org/10.1016/j.conbuildmat.2006.12.013.
[40] C.S. Poon, S.C. Kou, L. Lam, Influence of recycled aggregate on slump and bleeding of fresh concrete, Mater. Struct. 40 (2007) 981–988, https://doi.org/10.1617/s11527-006-9192-y.
[41] 2022, NF EN 1097-6, Tests for mechanical and physical properties of aggregates - Part 6: determination of particle density and water absorption.
[42] 2012, NF EN 933-1, Tests for geometrical properties of aggregates - Part 1: Determination of particle size distribution - Sieving method.
[43] 2020, NF EN 1097-2, Tests for mechanical and physical properties of aggregates - Part 2: Methods for the determination of resistance to fragmentation, 2.
[44] 2023, NF EN 1097-1, Tests for mechanical and physical properties of aggregates - Part 1: determination of the resistance to wear (micro-Deval).
[45] 2022, NF EN 1097-7, Tests for mechanical and physical properties of aggregates - Part 7: Determination of the particle density of filler - Pyknometer method.
[46] 2018, NF EN 196-6, Methods of testing cement - Determination of fineness.
[47] 2008, Tests for mechanical and physical properties of aggregates - Part 4: Determination of the voids of dry compacted filler, NF EN 1097-4.
[48] 2021, NF EN 15935, Soil, waste, treated biowaste and sludge - Determination ofloss on ignition.
[49] 2000, NF ISO 13320-1, Particle size analysis - Laser diffraction methods - Part 1: General principle.
[50] 2019, NF EN 12350-8, Testing fresh concrete - Part 8: Self-compacting concrete - Slump-flow test.
[51] R. Raydan, F. Chamseddine, A. Jahami, O. Baalbaki, J. M. Khatib, A. Elkordi, Production of low-cost self-consolidating concrete (SCC) using manufactured aggregates, BAU J. Sci. Technol. 3 (2022), https://doi.org/10.54729/HKRO9755.
[52] 2010, NF EN 12350-11, Testing fresh concrete - Part 11: Self-compacting concrete - Sieve segregation test.
[53] 2019, NF EN 12350-6, Testing fresh concrete - Part 6: density.
[54] 2010, NF EN 196-9, Methods of testing cement - Part 9: Heat of hydration - Semi-adiabatic method, (2010).
[55] 2019, NF EN 12390-3, Testing hardened concrete - Part 3: compressive strength of test specimens.
[56] 2022, NF P 18-459, Concrete - Testing hardened concrete - Density and porosity test.
[57] B.A. Tayeh, M.W. Hasaniyah, A.M. Zeyad, M.M. Awad, A. Alaskar, A. M. Mohamed, R. Alyousef, Durability and mechanical properties of seashell partially-replaced cement, J. Build. Eng. 31 (2020) 101328, https://doi.org/10.1016/J.JOBE.2020.101328.
[58] M.-Y. Xuan, H.-K. Cho, X.-Y. Wang, Performance improvement of waste oyster-shell powder–cement binary system via carbonation curing, J. Build. Eng. 70 (2023) 106336, https://doi.org/10.1016/j.jobe.2023.106336.
[59] L.P. Singh, A. Goel, S.K. Bhattachharyya, S. Ahalawat, U. Sharma, G. Mishra, Effect of morphology and dispersibility of silica nanoparticles on the mechanical behaviour of cement mortar, Int J. Concr. Struct. Mater. 9 (2015) 207–217, https://doi.org/10.1007/s40069-015-0099-2.
[60] H.F.W. Taylor, Cement chemistry, Thomas Telford London, 1997.
[61] J.F. Young, W. Hansen, Volume relationships for CSH formation based on hydration stoichiometries, MRS Online Proc. Libr 85 (1986) 313–322, https://doi.org/10.1557/PROC-85-313.
[62] ISO 15901-1, Evaluation of pore size distribution and porosity of solid materials by mercury porosimetry and gas adsorption - Part 1: Mercury porosimetry, (2016).
[63] D. Chateigner, C. Hedegaard, H.R. Wenk, Mollusc shell microstructures and crystallographic textures, J. Struct. Geol. 22 (2000) 1723–1735, https://doi.org/10.1016/S0191-8141(00)00088-2.
[64] R. Xing, Y. Qin, X. Guan, S. Liu, H. Yu, P. Li, Comparison of antifungal activities of scallop shell, oyster shell and their pyrolyzed products, Egypt J. Aquat. Res 39 (2013) 83–90, https://doi.org/10.1016/j.ejar.2013.07.003.
[65] D. Chateigner, S. Ouhenia, C. Krauss, C. Hedegaard, O. Gil, M. Morales, L. Lutterotti, M. Rousseau, E. Lopez, Voyaging around nacre with the X-ray shuttle: from bio-mineralisation to prosthetics via mollusc phylogeny, Mater. Sci. Eng A 528 (2010) 37–51.
[66] G. Rojo-López, B. González-Fonteboa, F. Martínez-Abella, I. González-Taboada, Rheology, durability, and mechanical performance of sustainable self-compacting concrete with metakaolin and limestone filler, Case Stud. Constr. Mater. 17 (2022) e01143, https://doi.org/10.1016/J.CSCM.2022.E01143.
[67] M. Hadjadj, M. Guendouz, D. Boukhelkhal, The effect of using seashells as cementitious bio-material and granite industrial waste as fine aggregate on mechanical and durability properties of Green flowable sand concrete, J. Build. Eng. 87 (2024) 108968, https://doi.org/10.1016/j.jobe.2024.108968.
[68] Y. Wu, J. Lu, Y. Nie, W. He, Effect of seashell powder as binder material on the performance and microstructure of low-carbon sustainable alkali-activated concrete, J. Build. Eng. 90 (2024) 109442, https://doi.org/10.1016/j.jobe.2024.109442.
[69] A.M. Zeyad, A. Almalki, Influence of mixing time and superplasticizer dosage on self-consolidating concrete properties, J. Mater. Res. Technol. 9 (2020) 6101–6115, https://doi.org/10.1016/J.JMRT.2020.04.013.
[70] Combined Effect of Polycarboxylate Ether and Phosphonated Superplasticizers in Limestone Calcined Clay Cement, in: SP-362: ICCM2024, American Concrete Institute, 2024. https://doi.org/10.14359/51741004.
[71] S. Moghul, F. Zunino, R.J. Flatt, Flow loss in superplasticized limestone calcined clay cement, J. Am. Ceram. Soc. 108 (2025), https://doi.org/10.1111/jace.20344.

[72] Z. Li, J. Liu, J. Xiao, P. Zhong, A method to determine water absorption of recycled fine aggregate in paste for design and quality control of fresh mortar, Constr. Build. Mater. 197 (2019) 30–41, https://doi.org/10.1016/J.CONBUILDMAT.2018.11.115.
[73] F. Azarhomayun, M. Haji, M. Shekarchi, M. Kioumarsi, Investigating the effectiveness of the stable measurement tests of Self-Compacting concrete, Constr. Build. Mater. 383 (2023) 131262, https://doi.org/10.1016/j.conbuildmat.2023.131262.
[74] M. Tuyan, A. Mardani-Aghabaglou, K. Ramyar, Freeze–thaw resistance, mechanical and transport properties of self-consolidating concrete incorporating coarse recycled concrete aggregate, Mater. Des. 53 (2014) 983–991, https://doi.org/10.1016/j.matdes.2013.07.100.
[75] H.R. Shadkam, S. Dadsetan, M. Tadayon, L.F.M. Sanchez, J.A. Zakeri, An investigation of the effects of limestone powder and viscosity modifying agent in durability related parameters of self-consolidating concrete (SCC), Constr. Build. Mater. 156 (2017) 152–160, https://doi.org/10.1016/J.CONBUILDMAT.2017.08.165.
[76] Md.H.R. Sobuz, S.D. Datta, A.S.M. Akid, V.W.Y. Tam, S. Islam, Md.J. Rana, F. Aslani, Ç. Yalçınkaya, N.M. Sutan, Evaluating the effects of recycled concrete aggregate size and concentration on properties of high-strength sustainable concrete, J. King Saud. Univ. Eng. Sci. (2022), https://doi.org/10.1016/j.jksues.2022.04.004.
[77] J.J. Assaad, J. Harb, Formwork pressure of Self-Consolidating concrete containing recycled coarse aggregates, Acids Mater. J. 114 (2017), https://doi.org/10.14359/51689494.
[78] C.-C. Liao, A study of the effect of liquid viscosity on density-driven wet granular segregation in a rotating drum, Powder Technol. 325 (2018) 632–638, https://doi.org/10.1016/j.powtec.2017.11.004.
[79] E.W.C. Lim, Density segregation of dry and wet granular mixtures in vibrated beds, Adv. Powder Technol. 27 (2016) 2478–2488, https://doi.org/10.1016/j.apt.2016.09.028.
[80] D. Zhao, J.M. Williams, Z. Li, A.-H.A. Park, A. Radlińska, P. Hou, S. Kawashima, Hydration of cement pastes with calcium carbonate polymorphs, Cem. Concr. Res 173 (2023) 107270, https://doi.org/10.1016/j.cemconres.2023.107270.
[81] L. Liu, P. Yang, C. Qi, B. Zhang, L. Guo, K.-I. Song, An experimental study on the early-age hydration kinetics of cemented paste backfill, Constr. Build. Mater. 212 (2019) 283–294, https://doi.org/10.1016/j.conbuildmat.2019.03.322.
[82] E. John, B. Lothenbach, Cement hydration mechanisms through time – a review, J. Mater. Sci. 58 (2023) 9805–9833, https://doi.org/10.1007/s10853-023-08651-9.
[83] M.M. Rusu, D. Faux, I. Ardelean, Monitoring the effect of calcium nitrate on the induction period of cement hydration via Low-Field NMR relaxometry, Molecules 28 (2023) 476, https://doi.org/10.3390/molecules28020476.
[84] P. Li, Z. Jiang, X. An, K. Maekawa, S. Du, Time-dependent retardation effect of epoxy latexes on cement hydration: experiments and multi-component hydration model, Constr. Build. Mater. 320 (2022) 126282, https://doi.org/10.1016/j.conbuildmat.2021.126282.
[85] X. PangThe effect of water-to-cement ratio on the hydration kinetics of Portland cement at different temperatures, in: Proceedings of the 14th International Congress on Cement Chemistry, 2015. https://doi.org/10.13140/RG.2.1.4526.2800..
[86] O. Oueslati, J. Duchesne, The effect of SCMs and curing time on resistance of mortars subjected to organic acids, Cem. Concr. Res 42 (2012) 205–214, https://doi.org/10.1016/J.CEMCONRES.2011.09.017.
[87] S. Ge, Y. Pan, L. Zheng, X. Xie, Effects of organic matter components and incubation on the cement-based stabilization/solidification characteristics of lead-contaminated soil, Chemosphere 260 (2020) 127646, https://doi.org/10.1016/J.CHEMOSPHERE.2020.127646.
[88] E. Lipczynska-Kochany, Humic substances, their microbial interactions and effects on biological transformations of organic pollutants in water and soil: a review, Chemosphere 202 (2018) 420–437, https://doi.org/10.1016/J.CHEMOSPHERE.2018.03.104.
[89] T. Danner, H. Justnes, M. Geiker, R.A. Lauten, Early hydration of C3A–gypsum pastes with Ca- and Na-lignosulfonate, Cem. Concr. Res 79 (2016) 333–343, https://doi.org/10.1016/J.CEMCONRES.2015.10.008.
[90] C. Ma, B. Chen, L. Chen, Effect of organic matter on strength development of self-compacting earth-based construction stabilized with cement-based composites, Constr. Build. Mater. 123 (2016) 414–423, https://doi.org/10.1016/J.CONBUILDMAT.2016.07.018.
[91] W. Maherzi, M. Benzerzour, Y. Mamindy-Pajany, E. van Veen, M. Boutouil, N. E. Abriak, Beneficial reuse of Brest-Harbor (France)-dredged sediment as alternative material in road building: laboratory investigations, Environ. Technol. 39 (2018) 566–580, https://doi.org/10.1080/09593330.2017.1308440.
[92] B. Tripathi, Effects of polymers on cement hydration and properties of concrete: a review, ACS Omega 9 (2024) 2014–2021, https://doi.org/10.1021/acsomega.3c05914.
[93] M.J. Ahmed, K. Lambrechts, X. Ling, K. Schollbach, H.J.H. Brouwers, Effect of hydroxide, carbonate, and sulphate anions on the β-dicalcium silicate hydration rate, Cem. Concr. Res 173 (2023) 107302, https://doi.org/10.1016/J.CEMCONRES.2023.107302.
[94] X. Gu, B. Yang, Z. Li, B. Liu, J. Liu, Q. Wang, M.L. Nehdif, Elucidating the reaction of seashell powder within Fly ash cement: a focus on hydration products, Constr. Build. Mater. 428 (2024) 136331, https://doi.org/10.1016/j.conbuildmat.2024.136331.
[95] E.A.B. Koenders, M. Pepe, E. Martinelli, Compressive strength and hydration processes of concrete with recycled aggregates, Cem. Concr. Res 56 (2014) 203–212, https://doi.org/10.1016/j.cemconres.2013.11.012.
[96] M. Pepe, E.A.B. Koenders, C. Faella, E. Martinelli, Structural concrete made with recycled aggregates: hydration process and compressive strength models, Mech. Res Commun. 58 (2014) 139–145, https://doi.org/10.1016/J.MECHRESCOM.2014.02.001.
[97] R. Hay, B. Peng, K. Celik, Filler effects of $CaCO_3$ polymorphs derived from limestone and seashell on hydration and carbonation of reactive magnesium oxide (MgO) cement (RMC), Cem. Concr. Res 164 (2023) 107040, https://doi.org/10.1016/j.cemconres.2022.107040.
[99] D.P. Bentz, A. Ardani, T. Barrett, S.Z. Jones, D. Lootens, M.A. Peltz, T. Sato, P. E. Stutzman, J. Tanesi, W.J. Weiss, Multi-scale investigation of the performance of limestone in concrete, Constr. Build. Mater. 75 (2015) 1–10, https://doi.org/10.1016/j.conbuildmat.2014.10.042.
[100] S. Bellara, W. Maherzi, S. Mezazigh, A. Senouci, Mineral waste valorization in road subgrade construction: Algerian case study based on technical and environmental features, Case Stud. Constr. Mater. 20 (2024) e02764, https://doi.org/10.1016/j.cscm.2023.e02764.
[101] E. Mahfoud, W. Maherzi, K. Ndiaye, M. Benzerzour, S. Aggoun, N.-E. Abriak, Mechanical and microstructural properties of just add water geopolymer cement comprised of Thermo-Mechanicalsynthesis Sediments-Fly ash mix, Constr. Build. Mater. 400 (2023) 132626, https://doi.org/10.1016/j.conbuildmat.2023.132626.
[102] A.D. Iams, M.Z. Gao, A. Shetty, T.A. Palmer, Influence of particle size on powder rheology and effects on mass flow during directed energy deposition additive manufacturing, Powder Technol. 396 (2022) 316–326, https://doi.org/10.1016/j.powtec.2021.10.059.
[103] P.L. Domone, Self-compacting concrete: an analysis of 11 years of case studies, Cem. Concr. Compos 28 (2006) 197–208, https://doi.org/10.1016/j.cemconcomp.2005.10.003.
[104] A. Hasnaoui, A. Bourguiba, N. Sebaibi, M. Boutouil, Valorization of queen scallop shells in the preparation of metakaolin-based geopolymer mortars, J. Build. Eng. 53 (2022) 104578, https://doi.org/10.1016/J.JOBE.2022.104578.
[105] G. İnan Sezer, Compressive strength and sulfate resistance of limestone and/or silica fume mortars, Constr. Build. Mater. 26 (2012) 613–618, https://doi.org/10.1016/j.conbuildmat.2011.06.064.
[106] D. Wang, C. Shi, N. Farzadnia, Z. Shi, H. Jia, Z. Ou, A review on use of limestone powder in cement-based materials: mechanism, hydration and microstructures, Constr. Build. Mater. 181 (2018) 659–672, https://doi.org/10.1016/j.conbuildmat.2018.06.075.
[107] S.-H. Choi, S.-E. Oh, J. Won, S.-Y. Chung, Impact of cleaning methods on the properties of cement mortars with cockle shell fine aggregates, Case Stud. Constr. Mater. 23 (2025) e05143, https://doi.org/10.1016/J.CSCM.2025.E05143.
[108] M. Fujishima, T. Miura, Y. Kawabata, Stress-bearing mechanism of concrete damaged by delayed ettringite formation under compressive stress with various loading patterns, J. Adv. Concr. Technol. 21 (2023) 294–306, https://doi.org/10.3151/jact.21.294.
[109] Z. Zhang, Y. Hu, L. Xiong, G. Geng, The influence of portlandite, calcite, quartz and ettringite inclusions on the multiscale mechanical behaviors of C-S-H matrix, Cem. Concr. Res 189 (2025) 107781, https://doi.org/10.1016/J.CEMCONRES.2024.107781.
[110] C. Martínez-García, B. González-Fonteboa, D. Carro-López, F. Martínez-Abella, Impact of mussel shell aggregates on air lime mortars. Pore structure and carbonation, J. Clean. Prod. 215 (2019) 650–668, https://doi.org/10.1016/J.JCLEPRO.2019.01.121.
[111] Y. Zhu, D. Chen, X. Yu, R. Liu, Y. Liao, Properties of cementitious materials utilizing seashells as aggregate or cement: prospects and challenges, Materials 17 (2024) 1222, https://doi.org/10.3390/ma17051222.
[112] A.G. Khoshkenari, P. Shafigh, M. Moghimi, H.Bin Mahmud, The role of 0–2mm fine recycled concrete aggregate on the compressive and splitting tensile strengths of recycled concrete aggregate concrete, Mater. Des. 64 (2014) 345–354, https://doi.org/10.1016/j.matdes.2014.07.048.
[113] W.C. Tang, P.C. Ryan, H.Z. Cui, W. Liao, Properties of Self-Compacting concrete with recycled coarse aggregate, Adv. Mater. Sci. Eng. 2016 (2016) 1–11, https://doi.org/10.1155/2016/2761294.
[114] J. Li, T. Wang, J. Hong, S. Liu, C. Zheng, Y. Chi, Axial compressive performance of low-carbon high-strength recycled aggregate concrete, Low. Carbon Mater. Green. Constr. 2 (2024) 25, https://doi.org/10.1007/s44242-024-00058-2.
[115] C. Wu, Y. Shi, J. Xu, M. Luo, Y. Lu, D. Zhu, Experimental study of mechanical properties and theoretical models for recycled fine and coarse aggregate concrete with steel fibers, Materials 17 (2024) 2933, https://doi.org/10.3390/ma17122933.
[116] C. Wang, C. Chazallon, S. Braymand, P. Hornych, Thermogravimetric analysis (TGA) for characterization of self-cementation of recycled concrete aggregates in pavement, Thermochim. Acta 733 (2024) 179680, https://doi.org/10.1016/j.tca.2024.179680.
[117] D.K. Panesar, B. Shindman, The effect of segregation on transport and durability properties of self consolidating concrete, Cem. Concr. Res 42 (2012) 252–264, https://doi.org/10.1016/j.cemconres.2011.09.011.
[118] J. Han, P. Yan, Influence of segregation on the permeability of self-consolidating concrete, Constr. Build. Mater. 269 (2021) 121277, https://doi.org/10.1016/J.CONBUILDMAT.2020.121277.
[119] K. Wu, H. Shi, G.De Schutter, G. Ye, Y. GaoMechanism of microstructural modification of the interfacial transition zone by using blended materials, in: 14th International Congress on the Chemistry of Cement (ICCC2015), 2015: pp. 1–11..

[120] A. Katz, Properties of concrete made with recycled aggregate from partially hydrated old concrete, Cem. Concr. Res 33 (2003) 703–711, https://doi.org/10.1016/S0008-8846(02)01033-5.
[121] D. Wang, C. Lu, Z. Zhu, Z. Zhang, S. Liu, Y. Ji, Z. Xing, Mechanical performance of recycled aggregate concrete in Green civil engineering: review, Case Stud. Constr. Mater. 19 (2023) e02384, https://doi.org/10.1016/j.cscm.2023.e02384.
[122] Y.F. Silva, S. Delvasto, S. Izquierdo, G. Araya-Letelier, Short and long-term physical and mechanical characterization of self-compacting concrete made with masonry and concrete residue, Constr. Build. Mater. 312 (2021) 125382, https://doi.org/10.1016/j.conbuildmat.2021.125382.
[123] E. Pahsha, P.S. Nair, R. Gupta, V. Agrawal, Sustainable development of self-compacting concrete incorporating granite waste and recycled concrete aggregate: evaluation of strength, durability, and microstructure, Sustain Chem. Pharm. 47 (2025) 102136, https://doi.org/10.1016/J.SCP.2025.102136.
[124] J.M.V. Gómez-Soberón, Porosity of recycled concrete with substitution of recycled concrete aggregate: an experimental study, Cem. Concr. Res 32 (2002) 1301–1311.
[125] Z.H. Duan, C.S. Poon, Properties of recycled aggregate concrete made with recycled aggregates with different amounts of old adhered mortars, Mater. Des. 58 (2014) 19–29, https://doi.org/10.1016/j.matdes.2014.01.044.
[126] B. El Moustapha, Effect of metakaolin addition on the mechanical performance and durability of granulated blast furnace slag based geopolymer mortar with Micro-Encapsulated phase change materials, J. Cem. Based Compos. 2 (2021) 23–31, https://doi.org/10.36937/cebacom.2021.001.005.
[127] B.El MoustaphaFormulation et étude d'un géopolymère accumulateur d'énergie thermique dans le cadre de l'éco-construction des bâtiments - PASTEL - Thèses en ligne de ParisTech, (2023). https://pastel.hal.science/tel-03965505/ (accessed August 28, 2025).
[128] D. Chen, T. Pan, X. Yu, Y. Liao, H. Zhao, Properties of hardened mortars containing crushed waste oyster shells, Environ. Eng. Sci. 36 (2019) 1079–1088, https://doi.org/10.1089/ees.2018.0465.
[129] R. Liu, J. Fan, X. Yu, Y. Zhu, D. Chen, Properties of mortar containing polyvinyl alcohol pretreated waste oyster shells with various concentrations, Constr. Build. Mater. 363 (2023) 129879, https://doi.org/10.1016/J.CONBUILDMAT.2022.129879.
[130] E. Baffoe, E. Dauer, A. Ghahremaninezhad, Effect of proteins on biocementation in construction materials, IScience 27 (2024) 108743, https://doi.org/10.1016/j.isci.2023.108743.
[131] C. Li, L. Jiang, Utilization of limestone powder as an activator for early-age strength improvement of slag concrete, Constr. Build. Mater. 253 (2020) 119257, https://doi.org/10.1016/J.CONBUILDMAT.2020.119257.
[132] Y.-S. Wang, S.-H. Tae, R.-S. Lin, X.-Y. Wang, Effects of Na_2CO_3 on engineering properties of cement–limestone powder–slag ternary blends, J. Build. Eng. 57 (2022) 104937, https://doi.org/10.1016/j.jobe.2022.104937.
[133] Z. Zhang, G. Geng, Measuring the surface cohesion of calcium silicate hydrate, Cem. Concr. Res 175 (2024) 107369, https://doi.org/10.1016/J.CEMCONRES.2023.107369.
[134] R. Shahrin, C.P. Bobko, Micropillar compression investigation of size effect on microscale strength and failure mechanism of Calcium-Silicate-Hydrates (C-S-H) in cement paste, Cem. Concr. Res 125 (2019) 105863, https://doi.org/10.1016/J.CEMCONRES.2019.105863.
[135] R. Alizadeh, J.J. Beaudoin, L. Raki, Mechanical properties of calcium silicate hydrates, Mater. Struct. 44 (2011) 13–28, https://doi.org/10.1617/s11527-010-9605-9.
[136] S. Zhang, R. Liu, C. Lu, Y. Gao, J. Xu, L. Yao, Y. Chen, Application of digital image correlation to study the influence of the water/cement ratio on the interfacial transition zone in cement-based materials, Constr. Build. Mater. 367 (2023) 130167, https://doi.org/10.1016/j.conbuildmat.2022.130167.
[137] A. Leemann, R. Loser, B. Münch, Influence of cement type on ITZ porosity and chloride resistance of self-compacting concrete, Cem. Concr. Compos 32 (2010) 116–120, https://doi.org/10.1016/j.cemconcomp.2009.11.007.
[138] I.G. Richardson, The nature of C-S-H in hardened cements, Cem. Concr. Res 29 (1999) 1131–1147, https://doi.org/10.1016/S0008-8846(99)00168-4.
[139] N.O. Emekli, M. Saydan, A. Ünal, Effect of hydration products on the mechanical behavior of reinforced concrete slabs made with ternary systems, J. Build. Eng. 106 (2025) 112625, https://doi.org/10.1016/j.jobe.2025.112625.
[140] X. Feng, J. Li, Q. Chen, J. Xu, G. Chen, Y. Sun, Z. Jiang, H. Zhu, Effect of flowing water on the ettringite-induced healing of concrete cracks by electrodeposition: experiments and molecular dynamics simulations, Constr. Build. Mater. 443 (2024) 137718, https://doi.org/10.1016/j.conbuildmat.2024.137718.
[141] Y. Chen, F. Al-Neshawy, J. Punkki, Investigation on the effect of entrained air on pore structure in hardened concrete using MIP, Constr. Build. Mater. 292 (2021) 123441, https://doi.org/10.1016/j.conbuildmat.2021.123441.
[142] T. Van Gerven, G. Cornelis, E. Vandoren, C. Vandecasteele, Effects of carbonation and leaching on porosity in cement-bound waste, Waste Manag. 27 (2007) 977–985, https://doi.org/10.1016/j.wasman.2006.05.008.
[143] R. Kumar, B. Bhattacharjee, Porosity, pore size distribution and in situ strength of concrete, Cem. Concr. Res 33 (2003) 155–164, https://doi.org/10.1016/S0008-8846(02)00942-0.
[144] S. Zhao, M. Xia, L. Yu, X. Huang, B. Jiao, D. Li, Optimization for the preparation of composite geopolymer using response surface methodology and its application in lead-zinc tailings solidification, Constr. Build. Mater. 266 (2021) 120969, https://doi.org/10.1016/j.conbuildmat.2020.120969.
[145] S. Bellara, M. Hidjeb, W. Maherzi, S. Mezazigh, A. Senouci, Optimization of an Eco-Friendly hydraulic road binders comprising clayey dam sediments and ground granulated Blast-Furnace slag, Buildings 11 (2021) 443, https://doi.org/10.3390/buildings11100443.
[146] B. Liu, X. Gu, H. Wang, J. Liu, M.L. Nehdi, Y. Zhang, Study on the mechanism of early strength strengthening and hydration of LC^3 raised by shell powder, J. Build. Eng. 98 (2024) 111422, https://doi.org/10.1016/J.JOBE.2024.111422.
[147] NF EN 206+A2/CN, 2022, Concrete - Specification, performance, production and conformity - National addition to the standard NF EN 206+A2.